



Publication Year	2015
Acceptance in OA @INAF	2020-03-04T15:54:13Z
Title	The Grism Lens-Amplified Survey from Space (GLASS). I. Survey Overview and First Data Release
Authors	Treu, T.; Schmidt, K. B.; Brammer, G. B.; Vulcani, Benedetta; Wang, X.; et al.
DOI	10.1088/0004-637X/812/2/114
Handle	http://hdl.handle.net/20.500.12386/23120
Journal	THE ASTROPHYSICAL JOURNAL
Number	812



THE GRISM LENS-AMPLIFIED SURVEY FROM SPACE (GLASS). I. SURVEY OVERVIEW AND FIRST DATA RELEASE

T. TREU^{1,2}, K. B. SCHMIDT², G. B. BRAMMER³, B. VULCANI⁴, X. WANG², M. BRADAC⁵, M. DIJKSTRA⁶, A. DRESSLER⁷, A. FONTANA⁸,
R. GAVAZZI⁹, A. L. HENRY¹⁰, A. HOAG⁵, K.-H. HUANG⁵, T. A. JONES², P. L. KELLY¹¹, M. A. MALKAN¹, C. MASON²,
L. PENTERICCI⁸, B. POGGIANTI¹², M. STIAVELLI³, M. TRENTI¹³, AND A. VON DER LINDEN^{14,15}

¹ Department of Physics and Astronomy, University of California, Los Angeles, CA 90095-1547, USA; tt@astro.ucla.edu

² Department of Physics, University of California, Santa Barbara, CA 93106-9530, USA

³ Space Telescope Science Institute, 3700 San Martin Drive, Baltimore, MD 21218, USA

⁴ Kavli Institute for the Physics and Mathematics of the Universe (WPI), The University of Tokyo Institutes for Advanced Study (UTIAS),
the University of Tokyo, Kashiwa, 277-8582, Japan

⁵ Department of Physics, University of California, Davis, CA 95616, USA

⁶ Institute of Theoretical Astrophysics, University of Oslo, P.O. Box 1029, NO-0315 Oslo, Norway

⁷ The Observatories of the Carnegie Institution for Science, 813 Santa Barbara Street, Pasadena, CA 91101, USA

⁸ INAF—Osservatorio Astronomico di Roma, Via Frascati 33, I-00040 Monte Porzio Catone, Italy

⁹ Institute d'Astrophysique de Paris, France

¹⁰ Astrophysics Science Division, Goddard Space Flight Center, Code 665, Greenbelt, MD 20771, USA

¹¹ Department of Astronomy, University of California, Berkeley, CA 94720-3411, USA

¹² INAF-Astronomical Observatory of Padova, Italy

¹³ School of Physics, University of Melbourne, VIC 3010, Australia

¹⁴ Dark Cosmology Centre, Niels Bohr Institute, University of Copenhagen Juliane Maries Vej 30, DK-2100 Copenhagen Ø, Denmark

¹⁵ Kavli Institute for Particle Astrophysics and Cosmology, Stanford University, 452 Lomita Mall, Stanford, CA 94305-4085, USA

Received 2015 May 14; accepted 2015 September 3; published 2015 October 14

ABSTRACT

We give an overview of the Grism Lens Amplified Survey from Space (GLASS), a large *Hubble Space Telescope* program aimed at obtaining grism spectroscopy of the fields of 10 massive clusters of galaxies at redshift $z = 0.308\text{--}0.686$, including the Hubble Frontier Fields (HFF). The Wide Field Camera 3 (WFC3) yields near-infrared spectra of the cluster cores covering the wavelength range $0.81\text{--}1.69\ \mu\text{m}$ through grisms G102 and G141, while the Advanced Camera for Surveys in parallel mode provides G800L spectra of the infall regions of the clusters. The WFC3 spectra are taken at two almost orthogonal position angles in order to minimize the effects of confusion. After summarizing the scientific drivers of GLASS, we describe the sample selection as well as the observing strategy and data processing pipeline. We then utilize MACSJ0717.5+3745, a HFF cluster and the first one observed by GLASS, to illustrate the data quality and the high-level data products. Each spectrum brighter than $H_{\text{AB}} = 23$ is visually inspected by at least two co-authors and a redshift is measured when sufficient information is present in the spectra. Furthermore, we conducted a thorough search for emission lines through all of the GLASS WFC3 spectra with the aim of measuring redshifts for sources with continuum fainter than $H_{\text{AB}} = 23$. We provide a catalog of 139 emission-line-based spectroscopic redshifts for extragalactic sources, including three new redshifts of multiple image systems (one probable, two tentative). In addition to the data itself, we also release software tools that are helpful to navigate the data.

Key words: gravitational lensing: strong

Supporting material: machine-readable table

1. INTRODUCTION

Over the past 25 years, the *Hubble Space Telescope* (*HST*) has assembled a phenomenal legacy of extragalactic surveys. Several legacy fields have been imaged at a variety of wavelengths, becoming the focus of ground-based telescopes and communities interested in intermediate- and high-redshift science (Ferguson et al. 2000; Giavalisco et al. 2004; Koekemoer et al. 2011; Scoville et al. 9; Ellis et al. 2013). Additionally, pure-parallel fields surveys have covered large uncorrelated areas providing even larger samples and means to control sample variance (Trenti et al. 2011; Colbert et al. 2013; Schmidt et al. 2014b).

A perhaps less well-known part of the *HST* legacy is the spectroscopic surveys carried out initially with the Near Infrared Camera and Multi-object Spectrograph (McCarthy et al. 1999) and the Advanced Camera for Surveys (ACS; Pirzkal et al. 2013), and more recently with the Wide Field Camera 3 (WFC3; Atek et al. 2010; Brammer et al. 2012;

Morris et al. 2015). By virtue of its low background and exquisite image quality compared to the ground, *HST* excels in low resolution slitless spatially resolved spectroscopy, particularly in the near-infrared. Thus, it has become a workhorse for galaxy evolution studies, including the following: the study of spatially resolved star formation (Nelson et al. 2012); the detection of rare galaxies with strong emission lines and faint continuum emission (Atek et al. 2011); and the measurement of absorption line redshifts for $z > 1$ galaxies (van Dokkum et al. 2011; Newman et al. 2013)

Current *HST* spectroscopic surveys have focused on relatively shallow spectroscopy of extragalactic fields. Although this is a very productive way to survey large areas of the sky, the target depth has typically been insufficient to address some of the most interesting questions in galaxy formation and evolution. For example, *HST* spectroscopic surveys have been able to detect Ly α for the brightest galaxies usually only during the tail-end of cosmic reionization (Rhoads

et al. 2013). Additionally, at lower redshifts, legacy fields and random parallels do not contain massive clusters of galaxies, and thus cannot probe the densest environments.

The fields of massive clusters of galaxies provide a very powerful complement to the traditional legacy fields. On the one hand they contain massive clusters of galaxies and thus enable the study of environmental effects. On the other hand the clusters themselves act as gravitational telescopes by magnifying objects in the background through the gravitational lensing effect. The lensing magnification enables the study of intrinsically fainter and more compact galaxies in the background than would be possible in empty fields at the expense of increased contamination by the foreground and a loss of cosmic volume for a fixed solid angle. It is important to stress that the net effect of a gravitational telescope on the number counts of a background population (sometimes known as magnification bias) can be both positive or negative, depending on the slope of the luminosity function: if the differential luminosity function is steeper than $dn/dL \propto L^{-2}$, one detects more objects behind a gravitational telescope, if it shallower the empty field has a higher yield (e.g., Meylan et al. 2006). In practice—at the bright end of the luminosity function where counts are rising exponentially—the net gain from lensing is huge and aids greatly in the detection of galaxies at $z > 6$. Even more importantly, for a fixed exposure time, lensing allows one to probe an intrinsically fainter population, thus providing qualitatively different insights into the source population.

Exploiting lensing magnification (Treu 2010; Coe et al. 2014) is one of the motivations behind many *HST* cluster surveys (e.g., Smith et al. 2001; Postman et al. 2012; Bayliss et al. 2014) and the main driver of the ongoing Hubble Frontier Field (HFF) initiative (J. Lotz et al. 2015, in preparation).

The Grism Lens Amplified Survey from Space (GLASS; PI Treu; GO 13459) has been designed and carried out in order to address some of the most compelling scientific questions by combining the power of deep *HST* spectroscopy with the magnification effect of gravitational lensing. The key science questions to be addressed by GLASS are the following.

1. How and when did galaxies reionize the universe (if they did)?
2. How do gas and metals cycle in and out of galaxies?
3. How does galaxy evolution depend on characteristics of the local environment?

First results on these topics are given in the papers by Schmidt et al. (2015), Jones et al. (2015), and B. Vulcani et al. (2015, in preparation).

In addition to the key questions driving the survey design, the data collected by GLASS enable the study of luminous and dark matter in the cluster themselves by providing spectroscopic redshifts of background sources to improve the lensing models, and provide additional epochs to search for high-redshift supernovae gravitationally lensed by the clusters. Examples of these two additional science goals are given in the early science papers by Schmidt et al. (2014b, hereafter paper 0), Kelly et al. (2015), and Wang et al. (2015).

In this paper we give an overview of GLASS and we present the first release of the data for MACS J0717.5+3745, the first cluster targeted by the survey. The paper is organized as follows. In Section 2 we review the scientific drivers of the survey. In Section 3 we give the rationale for selecting the sample of clusters and summarize their main properties. In

Section 4 we detail the observational strategy as well as the data reduction. In Section 5 we describe the postprocessing of the spectra, including procedure and tools for visual inspection and redshift determination. Section 7 concludes with a summary. Present and future data products are and will be made public through the *HST* archive. All magnitudes are given in the AB system and a standard concordance cosmology with $\Omega_m = 0.3$, $\Omega_\Lambda = 0.7$, and $h = 0.7$ is adopted when necessary.

2. SCIENTIFIC DRIVERS

2.1. Key Science Driver 1: Gas and Galaxies at the Epoch of Reionization

The universe is known to undergo dramatic evolution in the redshift range $z = 11$ – 6 while becoming fully ionized (Bennett et al. 2013; Mason et al. 2015; Planck Collaboration 2015; Robertson et al. 2015). However, how and when exactly it gets there is the topic of much debate. The interaction between the first galaxies and the intergalactic medium (IGM) is poorly understood, leaving many questions unanswered. How many ionizing photons escape from the local interstellar medium (ISM) into the IGM? What is the topology of the ISM/IGM at these redshifts? What is the relative contribution of galaxies vs active nuclei to ionizing budget (Madau et al. 2004; Ricotti & Ostriker 2004; Giallongo et al. 2015)?

The reduced observed Ly α flux from galaxies at $z > 6$ indicate that the process is still ongoing at $z \approx 6$ – 7 (e.g., McQuinn et al. 2007; Dijkstra et al. 2011; Jensen et al. 2013; Choudhury et al. 2014). This indication for “late” reionization is consistent with constraints derived from the Ly α forest (e.g., Becker et al. 2015) and also observed non-detection of the kSZ effect on small scales in the cosmic microwave background (Mesinger et al. 2012). In detail, quantitative constraints inferred from Ly α emitting galaxies still suffer significantly from observational uncertainties (e.g., Mesinger et al. 2015). In addition, uncertainties exist on the theoretical side which include how Ly α photons escape from galaxies, how this depends on galaxy properties, the role of galactic winds, and how much Ly α is reprocessed by the CGM (giving rise to “blobs/halos” see, e.g., Dijkstra 2014, for a review).

Recent ground-based observations suggest dramatic and rapid evolution of the IGM/ISM beyond $z \sim 6$. An important clue is that the fraction of dropouts that are Ly α emitters increases steadily out to $z \sim 6$ (e.g., Stark et al. 2011), while it declines significantly at $z \sim 7$ and above (Kashikawa et al. 2006; Fontana et al. 2010; Pentericci et al. 2011; Clément et al. 2012; Ono et al. 2012; Schenker et al. 2012; Treu et al. 2012, 2013). Large samples are now available at redshifts up to 7 where high-sensitivity multiplexed optical spectrographs can be used, and suggest that the IGM might indeed be partially neutral with a patchy distribution of Ly α optical depth (Pentericci et al. 2014, hereafter P14).

In contrast, spectroscopic follow-up at $z > 7$ has been very difficult, owing to the atmosphere which limits studies to a few specific redshift windows, in spite of the recent introduction of high sensitivity high multiplexed near-infrared spectrographs (e.g., MOSFIRE McLean et al. 2012). This difficulty is compounded by the weak average Ly α emission for the brighter continuum sources typically accessible with spectroscopy in legacy fields compared to the fainter ones (Stark et al. 2011).

The goal of GLASS is to target a large sample of intrinsically faint Lyman break galaxies (LBGs) at $z > 6.5$ in order to make

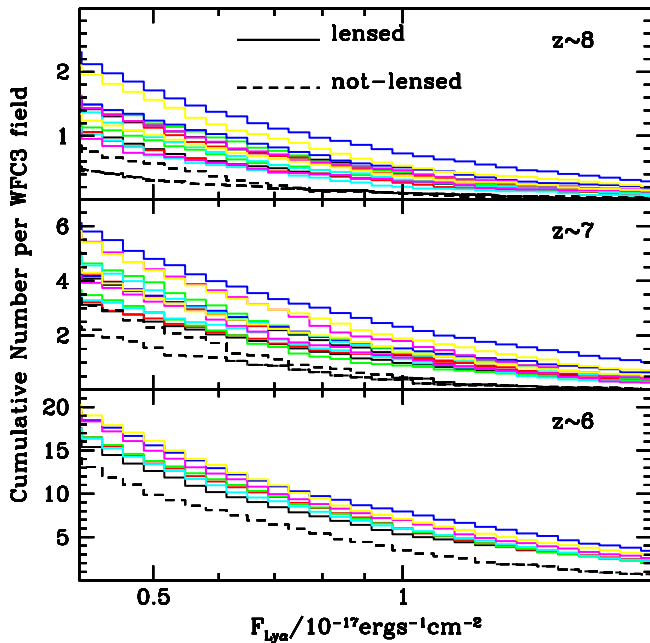


Figure 1. Predicted number of Ly α emitters per WFC3 field in cluster and blank fields based on the conditional probability function of Ly α emission for LBGs, and the LBG luminosity function model by Mason et al. (2015). Measuring the evolution of the luminosity function of Ly α emitters is one of the goals of GLASS. At the depth achievable with the WFC3, G102 grism lensing magnification has a positive effect at all relevant redshifts. The dashed lines are for blank fields, the solid lines are for specific GLASS clusters (A2744—black; A370—red; MACS0416—green; MACS0717—blue; MACS1149—cyan; RXJ1347—yellow; RXJ2248—magenta). At $z \sim 6$ the conditional probability distribution function is as described by Treu et al. (2012), based on the data by Stark et al. (2011). At $z \sim 7$ we use the two “patchy” measurements by Treu et al. (2012, upper curve of each pair) and Pentericci et al. (2014, lower curve) to give a sense of the measurement uncertainties. At $z \sim 8$ the conditional probability has been assumed to be the same as $z \sim 7$. More details on the models are given in the main text.

the most accurate measurement to date of the distribution of the Ly α optical depth, and thus probe the properties of the IGM/ISM. The first result of this investigation are discussed in detail by Schmidt et al. (2015). To achieve this goal GLASS exploits lensing magnification by the foreground clusters to reach fainter luminosities than would be possible in blank fields and thus in principle larger number of detections. Furthermore, theoretical (Zheng et al. 2011) and observational (Ouchi et al. 2009; Guaita et al. 2015) arguments indicate that high- z Ly α emitters might be significantly more spatially extended than the associated UV continuum. GLASS should provide the first constraints on the spatial extent of the Ly α emission on subarcsecond scales, via an individual study of magnified bright sources and a stacking analysis of the sample Schmidt et al. (2015).

2.1.1. Predicting the Ly α Number Counts

As a reference, Figure 1 shows the predicted number of dropouts as a function of Ly α flux. The forecast is based on three main ingredients: (i) the luminosity function of LBGs; (ii) the conditional probability of the Ly α equivalent width for LBGs of a given continuum magnitude; (iii) the distribution of magnifications provided by the foreground lensing clusters. For the first ingredient we use the model of the LBG LF recently proposed by Mason et al. (2015) building on earlier work by Trenti et al. (2010) and Tacchella et al. (2013). This model is in

excellent agreement with the actual number of LBGs detected in blank fields (e.g., Bradley et al. 2012; Oesch et al. 2013; Bouwens et al. 2014; Schmidt et al. 2014b). For the second ingredient we use the parametrization of the distribution of Ly α equivalent width introduced by Treu et al. (2012, hereafter T12). Based on data from the literature (Stark et al. 2011), at $z \sim 6$ the intrinsic rest-frame distribution is

$$p_6(W) = \frac{2A}{\sqrt{2\pi}W_c} e^{-\frac{1}{2}\left(\frac{W}{W_c}\right)^2} H(W) + (1-A)\delta(W), \quad (1)$$

with $W_c = 47 \text{ \AA}$, $A = 0.38$ for sources with $-21.75 < M_{\text{UV}} < -20.25$ and $W_c = 47 \text{ \AA}$, $A = 0.89$ for sources with $-20.25 < M_{\text{UV}} < -18.75$. A is the fraction of emitters, δ is the delta function, and H is the step function. As an illustration and to avoid overcluttering the figure, we consider here the “patchy” family of models introduced by T12, which appears to provide the best description of the data at $z \sim 7$. For this family of models, the intrinsic distribution of equivalent widths is expressed in terms of p_6 and the parameter ϵ_p :

$$\begin{aligned} p_p(W) &= \epsilon_p p_6(W) + (1 - \epsilon_p)\delta(W) \\ &= \frac{2A\epsilon_p}{\sqrt{2\pi}W_c} e^{-\frac{1}{2}\left(\frac{W}{W_c}\right)^2} H(W) + (1 - A\epsilon_p)\delta(W). \end{aligned} \quad (2)$$

As an illustration of the observational uncertainties, we consider two values of $\epsilon_p = 0.66, 0.46$, taken from T12 and P14, respectively. At $z \sim 8$, only upper limits are available (Treu et al. 2013). For simplicity we assume no evolution between $z \sim 7$ and $z \sim 8$, even though the number counts might be significantly lower at $z \sim 8$. In any case, the numbers are sufficiently large that a smaller number of detections at $z \sim 8$ would pose a stringent limit on the Ly α optical depth. For the third ingredient we use magnification maps based on grid-based weak and strong lensing models constructed by members of our team (e.g., Bradač et al. 2008; A. Hoag et al. 2015, in preparation; Wang et al. 2015), using the code developed by Bradač et al. (2005) in the adaptive version (Bradač et al. 2009). Those are available for 7/10 clusters at the moment of this writing, including both HFF and non-HFF clusters. These seven clusters are representative of the full GLASS sample, and therefore the range of magnification maps gives a good sense of range of expected variations from cluster to cluster. Mock catalogs of high-redshift galaxies are ray traced through the magnification maps to generate suitable mock catalogs in the image plane taking into account the boost in flux as well as the change in solid angle. The Ly α emission is assumed to be unresolved for this exercise, consistent with the observations (Schmidt et al. 2015).

The figure shows that magnification bias is positive in all cases, and cluster fields always yield more sources than blank fields, in the range of fluxes and redshifts considered here. Furthermore, there are cluster to cluster variations, but they are not extreme. This is due to the fact that the magnification effect of the most extreme lensing clusters, such as those in the HFF sample, is somewhat mitigated by the size of the field of view of WFC3. When the critical lines are larger than the WFC3 field of view, the high magnification areas can be lost to a single pointing campaign. As one can see from the range in the predictions, cluster to cluster variations are comparable to

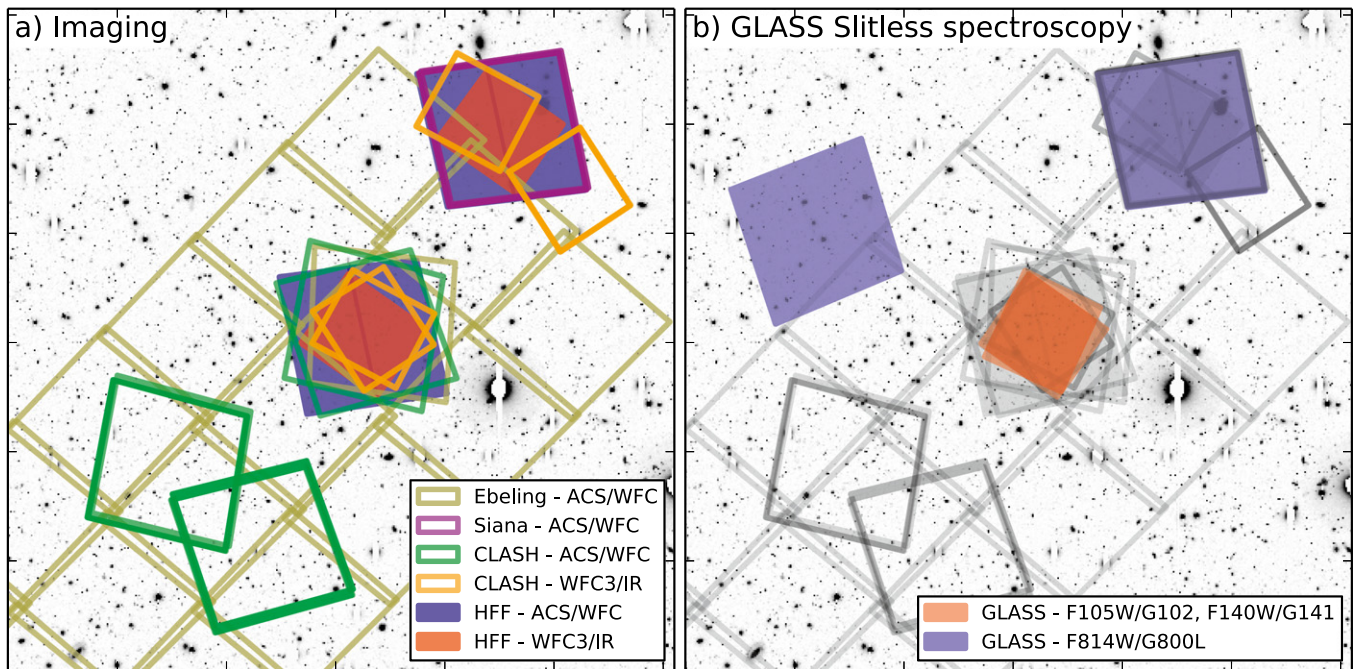


Figure 2. Observational layout of the GLASS spectroscopy in the context of existing imaging data for MACS J0717.5+3745. The WFC3 grism spectroscopy is aimed at the cluster center overlapping with deep multiband imaging from CLASH and/or HFF, while the two parallel fields are approximately 90° apart with one of them coinciding with the CLASH/HFF parallels.

current uncertainties on the distribution of equivalent width of $\text{Ly}\alpha$.

2.2. Key Science Driver 2: The Gas and Metal Cycles of Galaxies

How gas flows in and out of galaxies is a central question in galaxy formation and evolution as emphasized for example by the most recent Decadal Survey (Council 2010). The GLASS survey is particularly well suited for addressing gas flows at redshifts $z \simeq 2$, corresponding to the peak period of cosmic star formation rate density and hence rapid gas inflow and outflow rates (e.g., Shapley 2011; Madau & Dickinson 2014). We have identified a series of specific questions that can be addressed by GLASS in order to better understand the role of gas flows.

How do metallicity gradients evolve with cosmic time? Metallicity gradients are sensitive to the history of baryonic assembly: gas accretion, mergers, star formation, and outflows. Gradients measured from spatially resolved emission line diagnostics have provided significant insight into the assembly process at $z = 0$ (e.g., Vila-Costas & Edmunds 1992; Rupke et al. 2010; Bresolin et al. 2012). Cosmological simulations coupled with chemical evolution models can reproduce these data, but various models predict different behavior at earlier times (e.g., Pilkington et al. 2012; Gibson et al. 2013). Measurements for a large sample of galaxies over a range of redshift thus provide important constraints on galaxy assembly history (e.g., Troncoso et al. 2014).

How does the mass–metallicity–SFR relation evolve at low stellar mass? Local galaxies lie on a tight relation where metallicity increases with stellar mass (e.g., Tremonti et al. 2004) and typically decreases with SFR (e.g., Mannucci et al. 2010). Both effects can be explained by the cycling of gas and metals between galaxies and the IGM and are more pronounced at low mass. The cosmic evolution of this relation at low stellar mass is thus a powerful test of theories of feedback and of

metal enrichment of the IGM (e.g., Finlator & Davé 2008; Henry et al. 2013).

What causes the offset of star-forming galaxies in the BPT diagram (Baldwin et al. 1981) at high redshifts? Star-forming galaxies and active galactic nucleus (AGN) at $z = 0$ lie on separate well-defined loci in diagnostic line-ratio diagrams. High-redshift galaxies are often offset from the local star-forming locus toward that of AGN (Mannucci et al. 2010; Kewley et al. 2013; Shapley et al. 2014; Steidel et al. 2014). Spatially resolved data have shown that in some galaxies this is due to a combination of star formation and a weak active galactic nucleus (Wright et al. 2010; Trump et al. 2011), while others show pure star formation with offsets seen in individual giant star-forming regions (Jones et al. 2013b). Alternatively, recent work has shown that N-based indicators could be biased tracers of oxygen (Amorín et al. 2010; Andrews & Martini 2013; Masters et al. 2014; Shapley et al. 2015). Distinguishing these options is critical for metallicity studies.

Progress in measuring resolved emission line diagnostics at high redshift has been slow due to limitations in angular resolution and sensitivity. The most promising efforts, targeting gravitationally lensed galaxies with adaptive optics (AO), have yielded only a few metallicity gradients to date (Jones et al. 2010, 2013a; Yuan et al. 2013). Seeing-limited data have been obtained for larger samples (Queyrel et al. 2012; Troncoso et al. 2014) and are in tension with AO-based results, highlighting the need for high spatial resolution. The sensitivity of field *HST* surveys (e.g., WISP, 3D-*HST*, PEARS) is usually sufficient to study only the very brightest systems and their angular resolution does not benefit from lensing magnification.

The mass–metallicity–SFR relation has been measured by numerous groups in large samples extending to $z \simeq 3.5$ for the most massive ($M_* > 10^{9.5} M_\odot$) and luminous sources (e.g., Mannucci et al. 2010). Below $z \sim 1$, faint sources can be probed with optical spectra (Henry et al. 2013). At

higher redshifts, lensed galaxy surveys have extended this work to lower M_* and SFR (Belli et al. 2013), but are limited by small samples (i.e., only ~ 15 high redshift galaxies with $M_* < 10^9 M_\odot$). The vast majority of these studies rely on integrated spectra and therefore cannot distinguish the cause of offsets in the BPT diagram.

GLASS addresses these issues by collecting an unprecedented sample of emission line galaxies at $0.65 < z < 3.3$, with spatially resolved information for a significant fraction. The questions raised above are addressed via the integrated flux and spatial distribution of multiple emission line diagnostics which are sensitive to the gas metallicity and ionizing source. In particular the strong lines [O II], [O III], and $H\beta$ are all observed for galaxies at $1.3 < z < 2.3$ providing good diagnostics of both metallicity and nuclear activity (for example via the “blue” diagnostic diagram; Lamareille 2010). [S II] and $H\alpha + [N II]$ are also valuable diagnostics available at $z < 1.5$, while metallicities can still be estimated for the strongest line emitters at $2.3 < z < 3.3$ via [O II] and [Ne III]. As shown by Jones et al. (2015), the quality of the GLASS data enables accurate measurements of metallicity gradients, and of the mass–metallicity–SFR relation down to $M_* = 10^7 M_\odot$ at $z = 2$. This progress is made possible by the observing strategy and lensing magnification which deliver an order of magnitude improvement in flux sensitivity and an order of 3–4 in spatial resolution over previous *HST* grism surveys in blank fields (e.g., Henry et al. 2013). In general, the broad wavelength coverage of GLASS enables the comparison of metallicity estimates based on different features, so that one can test, for example, whether the [N II]-based estimates are biased with respect to [S II].

2.3. Key Science Driver 3: Environmental Dependence on Galaxy Evolution

The epoch $0 < z < 1$ is one of rapid decline in the global star formation rate (Lilly et al. 1996; Madau et al. 1996; Madau & Dickinson 2014), but clusters experience an evolution in star formation activity over this time that is even stronger than the general field. Identifying the processes that trigger and terminate star formation in cluster galaxies (Butcher & Oemler 1984; Dressler et al. 1999, 2013; Poggianti et al. 1999), and contrasting them to those operating in the field (Cooper et al. 2008; Vulcani et al. 2010; Muzzin et al. 2012; Oemler et al. 2013) is key to understanding the causes of the general decline. For what galaxy types and masses are environmental effects driving the quenching of star formation, and what is instead internally driven (Peng et al. 2010)? Is there one process that dominates over all environments or do some play a larger role in driving galaxy evolution in the field than they do in dense environments? Massive clusters are the sites where the effects of environmental processes, such as ram pressure stripping, are expected to be strongest. Hence, studies of massive clusters are needed to answer these questions.

Each of the processes that have been proposed to quench star formation in galaxies should leave a different signature on the spatial distribution of the star formation activity within the galaxy. As an example, the loss of the galaxy hot gas halo would lead to a suppression of star formation over the whole disk, while ram-pressure stripping should leave a recognizable pattern of star formation with truncated $H\alpha$ disks smaller than the undisturbed stellar disk (see Yagi et al. 2015, for an example of ram pressure stripping). What is needed is thus an

unbiased census of the star formation activity in a statistically significant sample of clusters, yielding both the total star formation rates and the spatial distribution of star-forming regions within galaxies. A most interesting epoch for such a study is in the range $z \sim 0.3$ –1 where most of the evolution takes place.

$H\alpha$ is considered the best optical indicator of the current star formation rate, as it is much less affected by dust extinction and metallicity effects than [O II] (Kennicutt 1998; Moustakas et al. 2006). For this reason, a number of $H\alpha$ surveys up to $z \sim 1$ have been undertaken in the field using narrow-band imaging (e.g., Sobral et al. 2013) and with WFC3 grism observations (e.g., Atek et al. 2010; Straughn et al. 2011). In clusters, narrow-band $H\alpha$ studies are available for just a few systems at $z = 0.3$ –1 (Kodama et al. 2004; Finn et al. 2005; Koyama et al. 2011) and a few other higher- z overdense regions (Koyama et al. 2013). These studies provide integrated $H\alpha$ fluxes, and no spatial distribution information. The power of spatially resolved information is exemplified by a study of Virgo which suggested that in the local universe stripping of gas is the main mechanism for quenching star formation rates in clusters (Koopmann & Kenney 2004).

GLASS is designed to measure $H\alpha$ fluxes for all cluster star-forming galaxies in the central 0.6–0.9 Mpc of 10 clusters at $z = 0.31$ –0.69. Note that $H\alpha$ and [N II] are blended at the resolution of G102; this effect can be taken into account when comparing with other samples, or corrected based on higher spectral resolution data (Trump et al. 2011, 2013; Fumagalli et al. 2012). GLASS’s target sensitivity is an order of magnitude improvement over previous studies of emission lines in cluster galaxies (Sobral et al. 2013). GLASS is designed to reach SFR limits comparable to the deepest narrow band studies, but for all objects and with spatially resolved information (see B. Vulcani et al. 2015, in preparation, for more details). Thus, GLASS is the first unbiased source of spatially resolved star formation within cluster galaxies at these redshifts. The combination of GLASS spectroscopy and *HST* photometry from CLASH/HFF is used to identify uniquely the line as $H\alpha$, as well as measure morphology, spatially resolved colors and stellar masses for virtually all objects detected in emission.

Parallel ACS G800L Grism spectroscopy in two offset fields (at 2–3 Mpc, i.e., 1–3 virial radii; 2 position angles; see Figure 2) for each cluster, will cover the cluster infall regions, a key region for some environmental processes (e.g., Treu et al. 2003). In these regions $H\beta$ (and [O II] at $z > 0.6$) can be used as star formation indicators, while [O III] further aids in redshift identification. By combining cluster cores, infall regions, and field, GLASS enables the study of the spatially resolved star formation across a wide range of environments. Given the low number density of cluster members at such clustercentric distances, the ACS grism is the ideal method to build complete samples of star-forming galaxies. The parallel ACS data are not part of this first data release and will be discussed in detail in future publications.

2.4. Additional Science Drivers

GLASS spectroscopy and imaging is suitable for a wide range of applications. Although the survey design is driven by the three science cases described above, two additional science drivers were taken into account when possible. They are briefly summarized below.

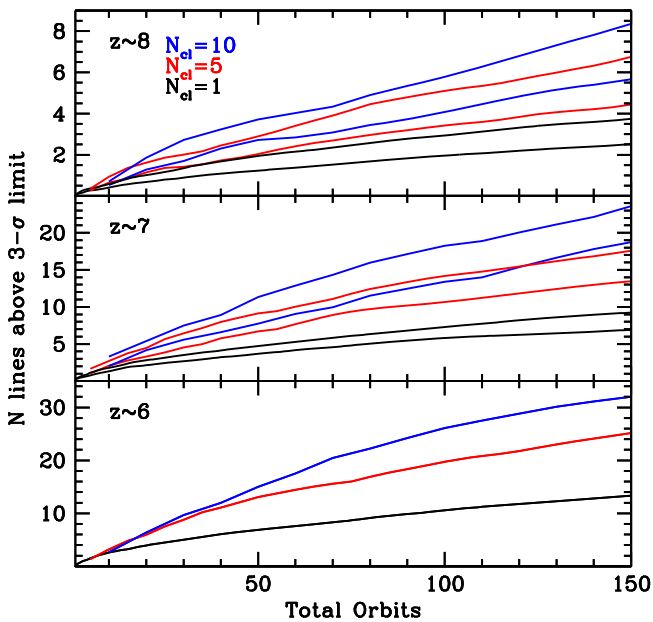


Figure 3. Number of Ly α lines with flux above $3\text{-}\sigma$ as a function of total G102 orbits divided over N_{cl} clusters. Once a sufficient depth is reached, the number of detection increases linearly with the number of clusters and less rapidly with exposure time owing to the loss of efficiency in magnification bias in addition to the normal scaling of noise and number counts observed in empty fields. The predictions are based on the model shown in Figure 1 and described in the main text. Only the results for cluster RXJ1347 are shown for clarity. At $z \sim 7$ and 8 the upper and lower lines of each color represent $\epsilon_p = 0.66$ and $\epsilon_p = 0.46$ respectively, as in Figure 1.

2.4.1. Luminous and Dark Matter in Clusters of Galaxies

Measuring the distribution of matter in clusters of galaxies is a powerful way to address a number of fundamental astrophysical questions, ranging from cosmology to the interaction between supermassive black holes and their environment. What is the self-interaction cross section of dark matter? Is dark matter cold? What is the net effect of energy feedback from black hole accretion on dark matter halos?

By modeling the gravitational lensing distortion of background galaxies one can obtain precise and accurate two-dimensional maps of the mass distribution in the clusters themselves. Considerable effort has gone and is going into developing modeling techniques that exploit all the available information, and deep *HST* imaging data have allowed researchers to identify more than one hundred multiple images of background sources per clusters. However the vast majority of these multiple images do not have spectroscopic redshift identification, and photometric redshift must be used to transform their positions into constraints on the gravitational potential of the clusters. Spectroscopic redshifts help enormously by reducing the effective uncertainty of each potential measurement to below 1% and by eliminating mis-identifications and catastrophic errors on photo- z which are common for extremely faint galaxies with unusual shapes. One of the ancillary drivers of GLASS is to measure spectroscopic redshifts for as many faint sources as possible in order to provide more extended and cleaner catalogs of multiple images to be used as input to lens models. First examples of this application of GLASS are given by Schmidt et al. (2014a) and Wang et al. (2015).

2.4.2. Supernovae

Gravitational telescopes magnify all sources in the background, including transient ones. Thus, in principle, gravitational telescopes can be used to detect and take spectra of supernovae that are fainter and more distant than otherwise possible (Brammer et al. 2014a), thus extending the look back time over which supernovae and supernova cosmology can be studied (e.g., Sullivan et al. 2000; Patel et al. 2014). If the lensed supernovae are of type Ia, knowledge of their absolute magnitude provides an opportunity to break the mass-sheet degeneracy (Nordin et al. 2014; Zitrin et al. 2014; Rodney et al. 2015).

In rare circumstances, if the supernovae happens to explode within the cluster’s caustics, the supernovae can appear multiply imaged to the observer. The difference in arrival time between the images is measurable and can be used as a cosmic ruler to measure distances and hence cosmology (Refsdal 1964; Holz 2001; Bolton & Burles 2003), provided the gravitational potential of the cluster can be sufficiently well constrained. This technique has been demonstrated to be very powerful using quasars as the variable lensed source. Typically, the deflectors are galaxies, for which the gravitational potential can be sufficiently well constrained by extended gravitational arcs and stellar kinematics (Treu & Koopmans 2002; Suyu et al. 2014). Multiply imaged supernovae are significantly more difficult to find, and the first example has been discovered only recently in data taken by the GLASS survey (Kelly et al. 2015).

This area of science has been done in close coordination with the FrontierSN Program (GOs 13386 and GO 13790; PI: Rodney) for the HFF clusters, ensuring uniform acquisition and analysis of the data.

3. SAMPLE SELECTION AND PROPERTIES

The number and choice of clusters depend on a number of factors, starting from the steepness of the number counts of the target population. The epoch of reionization science driver was used to select the optimal strategy. Figure 3 shows the expected number of Ly α emitters as a function of *total* number of orbits, using the model described in Section 2.1.1, plus the actual sensitivity measured for the GLASS grism data.¹⁶ At $z \sim 6\text{--}8$, once a sufficient depth per cluster is reached, the number of sources is maximized by observing more clusters rather than going deeper. Observing multiple clusters also minimizes cosmic variance (for $z > 6$ galaxies $\lesssim 10\%$ for 10 clusters, compared to 30% for a single WFC3 field, Trenti & Stiavelli 2008). Observing only four clusters (e.g., the initial HFF targets) for a longer individual exposure reduces the number of detections because magnification becomes less effective. Of course, even though we chose the number of sources as metric, this is not the only reasonable choice. By going deeper on a smaller number of clusters one would have probed an intrinsically different population of galaxies.

In order to find the 10 best clusters to target with GLASS we turned to the CLASH and HFF initiatives for the unique data that are being accumulated by a variety of groups with *HST* and other facilities. This vast array of data makes the identification of emission lines much easier than for clusters with just a few *HST*

¹⁶ As it will be shown later in the paper, the sensitivity to Ly α varies very rapidly between $z = 5.5$ and 6.5. We are taking as a reference the value at $z = 6$, although most objects will be detected above $z > 6$ where the sensitivity is highest.

Table 1
Sample Properties

Cluster	R.A. (J2000)	decl. (J2000)	z	<i>HST</i> Imaging	<i>Spitzer</i> Imaging	L_X (10^{44} erg s $^{-1}$)	M_{500} ($10^{14} M_\odot$)	First Release
A2744	00:14:23.4	−30:23:26	0.308	HFF1	SFF	15.28 ± 0.39	17.6 ± 2.3	F15
A370	02:39:52.8	−01:34:36	0.375	HFF3	SFF	8.56 ± 0.37	11.7 ± 2.1	W16
M0416.1−2403	04:16:09.4	−24:04:04	0.420	CLASH/HFF1	SURFSUP	8.11 ± 0.50	9.1 ± 2.0	W16
M0717.5+3745	07:17:31.6	+37:45:18	0.548	CLASH/HFF2	SFF	24.99 ± 0.92	24.9 ± 2.7	This paper
M0744.9+3927	07:44:52.8	+39:27:24	0.686	CLASH	SURFSUP	18.94 ± 0.61	12.5 ± 1.6	W16
M1149.6+2223	11:49:35.9	+22:23:55	0.544	CLASH/HFF2	SURFSUP	17.25 ± 0.68	18.7 ± 3.0	F15
RXJ1347.5−1145	13:47:30.6	−11:45:10	0.451	CLASH	SURFSUP	47.33 ± 1.2	21.7 ± 3.0	S15
M1423.8+2404	14:23:47.8	+24:04:40	0.545	CLASH	SURFSUP	13.96 ± 0.52	6.64 ± 0.88	S15
M2129.4−0741	21:29:26.1	−07:41:29	0.570	CLASH	SURFSUP	13.69 ± 0.57	10.6 ± 1.4	S15
RXJ2248	22:48:44.3	−44:31:36	0.348	CLASH/HFF3	SFF	30.81 ± 1.57	22.5 ± 3.3	S15

Notes. For each cluster we list J2000 coordinates, redshift, the main sources of *HST* and *SST* imaging, as well as M_{500} from M_{gas} and X-ray luminosity (from Mantz et al. 2010). The last column lists the target date for the first public data release (F—Fall, S—Summer, W—Winter).

filters, e.g., allowing for the use of the dropout technique to confirm that a single emission line is indeed $\text{Ly}\alpha$, and of photo- z s to resolve cases with multiple line identifications. We further pruned the list of GLASS and CLASH clusters, using cluster redshift as an additional criterion. In fact, clusters at $z \approx 0.3$ – 0.8 are the best gravitational telescopes for two reasons: (i) the size of the critical lines is well matched to the WFC3 field of view; (ii) cluster galaxies appear smaller and fainter than in lower redshift clusters, thus minimizing the foreground contamination for background sources. The final requirement is given by the ability to observe $\text{H}\alpha$ in cluster galaxies ($z = 0.22$ – 1.59). Based on these criteria we selected the sample of ten clusters at $z = 0.31$ – 0.69 listed in Table 1. The table lists the main (but not only) sources of *HST* imaging and *Spitzer* Imaging, as well as basic features like redshift, X-ray temperature and weak lensing virial mass. Much ancillary data is available for these clusters at virtually all wavelengths.

4. OBSERVATIONS AND DATA REDUCTION

The two grisms G102 and G141 provide continuous wavelength coverage in the range 0.81 – $1.69 \mu\text{m}$ (defined as the range where the sensitivity is $>20\%$ of the peak), thus enabling the detection of $\text{Ly}\alpha$ above $z = 5.7$, metallicity gradients over a range of redshifts, and $\text{H}\alpha$ for the cluster members (see Figure 4).

The depth of 10 orbits in G102 was driven by the need to reach a sensitivity sufficient to probe the $\text{Ly}\alpha$ luminosity function at $z \gtrsim 6$. The depth of four orbits in G141 was chosen to reach approximately uniform sensitivity across the two grisms, which is appropriate to measure typical line ratios required for metallicity determinations (Atek et al. 2010; Henry et al. 2013). In this section we detail the observational strategy (4.1) and the data reduction process (4.2).

4.1. Phase II Design

The main pointing was chosen to overlap with existing or planned *HST* imaging observations. The observations of each cluster were then divided into two sets of visits at different roll angles, to help dealing with the effects of contamination in the crowded cluster fields. One position angle was chosen so that its ACS parallel field would land in a HFF or CLASH parallel field, while the second roll angle was chosen to be at $90^\circ \pm 10^\circ$ from the first, so as to resolve contamination from overlapping

spectra, while maximizing the overlap between the two WFC3 grism pointings.

A dither strategy analogous to that followed by the 3D-*HST* survey shown in Figure 3 of Brammer et al. (2012) has been adopted, in order to maximize spatial and spectral resolution and defect removal. For each visit at least four subexposures were taken for each grism (typically half orbit each) with semi-integer pixel offsets, so that they could be combined by interlacing as described in the next section.

A paired direct image exposure was taken with each grism exposure (F105W or F140W for G102 or G141, respectively) without offsetting the telescope for image alignment and spectral calibration. For visits that contained only G102 spectroscopy, some of the pre-imaging was obtained in F140W in order to ensure uniform filter coverage of transient events like Supernovae. This choice had virtually no impact of the depth of the F105W exposures or accuracy of the calibration of the G102 spectroscopy while at the same time assisting for the ancillary science case. Furthermore, after aligning the grism visits to existing observations from the CLASH and HFF programs, the deeper images from those programs can be used as the reference for the spectral extractions and modeling.

The effective exposure times for MACSJ0717.5+3745 in G102, G141, F105W, and F140W at the two different position angles are listed in Table 2 and are typical of all GLASS clusters. The notional depth of the G102 and G141 grism exposures are 10 and 4 orbits, respectively, including alignment images and overheads.

The depth of the spectroscopic data is illustrated in Figure 5 which gives the sensitivity for an unresolved emission line in a clean part of the field of view. The sensitivity estimates were estimated for a sample of non-detections $z \gtrsim 7$ compact dropouts from the first six GLASS clusters as presented by Schmidt et al. (2015). We used extraction apertures of 5 (spatial) by 3 (spectral) native pixels, which corresponds to apertures of $\sim 0''.6 \times 100 \text{ \AA}$, similar to what was used by Schmidt et al. (2014a). For more extended emission and larger objects, a larger aperture of, e.g., 10 (spatial) by 6 (spectral) native pixels, might be more representative of the sensitivity estimates. Such an aperture will increase the noise level by a factor of two. These noise levels are in fair agreement with previously published sensitivities of the *HST* NIR grisms (Brammer et al. 2012; Trump et al. 2014). We note that the

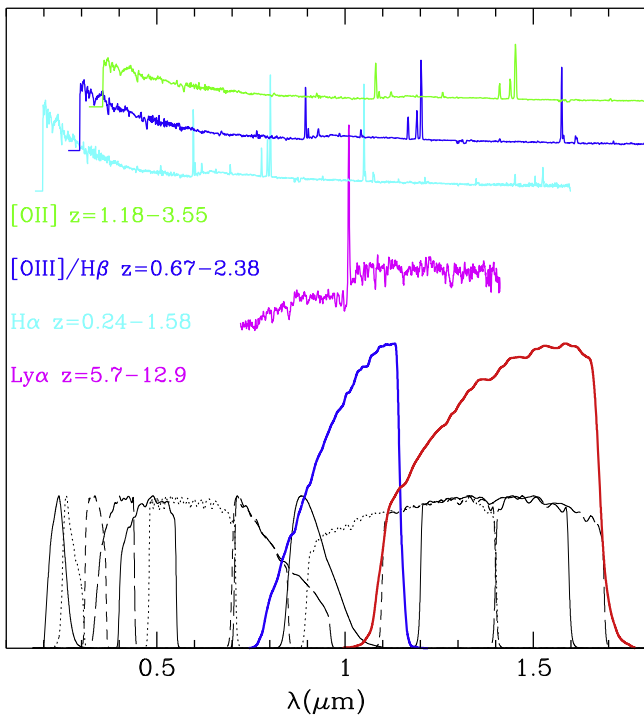


Figure 4. Illustration of the wavelength coverage provided by the two WFC3 grism (in red and blue, respectively, G141 and G102). The continuous wavelength coverage between ~ 0.81 – $1.69 \mu\text{m}$ enables all three main science drivers. The transmission curves of the filters used by the CLASH imaging program are shown as light black curves for comparison. Four example spectra, one for each of the diagnostic features shown in the caption, are overplotted for illustration.

Table 2
MACS J0717.5+3745 Exposure Times

Filter	P.A. = 20	P.A. = 280	Total
	$t_{\text{exp}}/(\text{s})$	$t_{\text{exp}}/(\text{s})$	
G102 ^a	9629	10829	20459
G141 ^a	3812	4312	8123
F105W	1979	1979	3959
F140W	712	712	1423

Notes. The exposure times for MACS J0717.5+3745 are typical of the GLASS data set for all 10 clusters. The position angles listed correspond to the *HST* keyword PA_V3. The P.A. of the y-axis corresponds to PA_V3+44.69. Additional imaging data are available from the *HST* archive.

^a Exposure times after correction for He Earth-glow (see Section 4.2).

depth of the spectroscopic data varies significantly from cluster to cluster owing to the variable background level, due to the combined zodiacal light and atmospheric emission.

The depth of the imaging data is comparable to that of CLASH. All imaging data obtained as part of the GLASS program are combined with imaging data taken as part of the CLASH and HFF programs.

4.2. Data Reduction

As noted in Section 4.1, the GLASS observations are designed to comply with the 3D-*HST* observing strategy and were processed with an updated version of the 3D-*HST* reduction pipeline¹⁷ described by Brammer et al. (2012). The

¹⁷ <http://code.google.com/p/threedhst/>

updated pipeline combines the individual exposures into mosaics using AstroDrizzle (Gonzaga et al. 2012), replacing the MultiDrizzle package (Koekemoer et al. 2003) used in earlier versions of the pipeline. The individual exposures and visits are aligned using *tweakreg* and grism sky backgrounds are subtracted using master sky images as described by G.B. Brammer (2015, in preparation), Kümmel et al. (2011), and Brammer et al. (2012). The direct images were sky subtracted by fitting a second-order polynomial to each of the source-subtracted exposures. Each exposure is then interlaced to a final image with a pixel size of $\approx 0''.06 \times \sim 12(22) \text{ \AA}$ for the G102 (G141) grisms. Before sky-subtraction and interlacing each individual exposure was checked and corrected for elevated backgrounds due to the He Earth-glow described by Brammer et al. (2014b). The pipeline is re-run in a way that does not flag bad reads as cosmic rays, as discussed by G.B. Brammer (2015, in preparation), using the script available here https://github.com/gbrammer/wfc3/blob/master/reprocess_wfc3.py. The final interlaced and sky-subtracted mosaics of the G102 and G141 grism for the two GLASS position angles are shown in the 4 bottom panels of Figure 6.

From these final mosaics, the spectra of each individual object are extracted by predicting the position and extent of each two-dimensional spectrum based on the SExtractor (Bertin & Arnouts 1996) segmentation of the corresponding direct images. As this is done for every single object, the contamination, i.e., the dispersed light from neighboring objects in the direct image field of view, can be estimated and accounted for. We note that a complete description of the 3D-*HST* image preparation pipeline, spectral extractions, and spectral fitting, will be provided by I.G. Momcheva et al. (2015, in preparation).

5. DATA QUALITY, VISUAL INSPECTION, AND CONSTRUCTION OF THE REDSHIFT CATALOG

Given the richness and complexity of the data set, we find that visual inspection of a magnitude-limited subset of the data is a very useful addition to the automatic processing. It was decided to carry out visual inspection of the redshift determinations as well, in order to flag catastrophic failures in the automated redshift determination. The automated redshift determination and subsequent visual inspection are described in Section 5.2. In addition to the complete magnitude-limited catalogs we also carried out a visual search for isolated emission lines through the entire data set. This search yielded additional redshifts and is described in Section 5.3.

5.1. Visual Inspection Strategy

Visual inspection carried out with the publicly available Graphic User Interface GIG (GLASS Inspection GUI) is described in the Appendix. GIG provides a convenient and efficient way to browse the data set. The inspection is aimed at assessing the quality of the data and it is therefore independent of any additional analysis like photometric redshifts.

The main goals of the GLASS team visual inspection were the following.

1. Identify and flag catastrophic failures of the pipeline. Even though these are rare in numbers, they can create substantial problems in subsequent analysis if they are not properly flagged. Examples include systematic errors

Table 3
Redshift Catalog

ID ^a	R.A. (J2000)	decl. (J2000)	z	Quality	Mult	Notes
036	109.39293627	37.77049774	0.0000	4.0	0.0	star
055	109.39810224	37.770416861	0.8785	3.5	0.0	...
057	109.40038631	37.770271353	0.0000	3.0	0.0	star
145	109.40230016	37.766627582	1.3575	2.0	0.0	...
173	109.39848457	37.766442326	0.5560	3.0	0.5	...
234	109.39639585	37.764684116	0.5490	4.0	0.0	...
236	109.39366519	37.764470231	0.3900	4.0	0.0	...
272	109.39400607	37.764400472	0.3895	4.0	0.0	...
273	109.40514662	37.764210184	0.0000	4.0	0.0	star
299	109.39108321	37.763095453	1.9000	1.5	0.0	...
307	109.39619713	37.76335404	2.5400	4.0	1.0	image 13.3

Notes. First entries of the redshift catalog. The full catalog is given in its entirety in the electronic edition. The column “quality” contains the quality flag as described in the text. The column “mult” is set to one when a single line is detected and there are multiple possible redshift interpretations. The column “note” lists special comments about the object, e.g., if the object is part of a known multiply image system.

^a In the final catalog ids are formatted as either 0xxxx or 9xxxx. The IDs with a leading 9 refers to a reduction, which used more aggressive SExtractor de-blending and detection parameters. This was done to accommodate the detection of objects near bright objects, which are not assigned individual IDs when using the CLASH SExtractor parameter file (IDs with a leading 0).

(This table is available in its entirety in machine-readable form.)

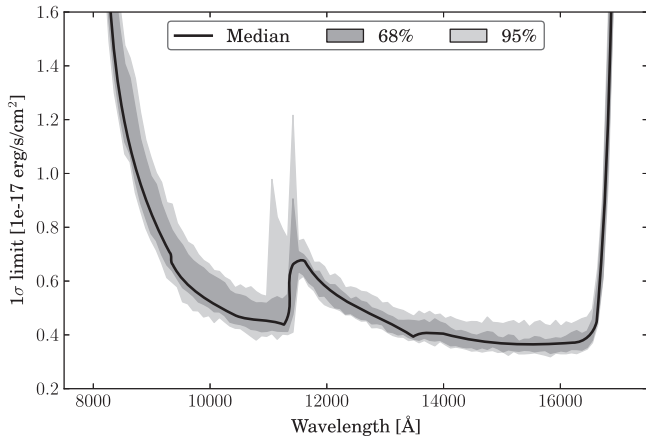


Figure 5. Observed 1σ noise level (not accounted for lensing magnification) for a sample of non-detections high- z dropouts from the first six GLASS clusters (see Schmidt et al. 2015 for details). An extraction parameter of approximately $0''.6 \times 100 \text{ \AA}$ running over the full G102+G141 wavelength range was used. Due to significantly varying contamination for individual objects between the two observed GLASS position angles, the noise level is shown for spectra extracted from a single P.A. Hence, the displayed limits correspond to the depth obtained from half of the GLASS data on each object. Combining spectra at the two P.A. for contamination free wavelength ranges will lower the noise level by a factor of $\sqrt{2}$. For more extended galaxies, more representative noise levels can be obtained using a larger extraction aperture, e.g., of $1''.2 \times 200 \text{ \AA}$, which will decrease the sensitivity by a factor 2.

in the reconstruction of the contamination spectra and artifacts due to edge effects.

2. Assess the degree of contamination in the spectra. The degree of contamination of a spectrum depends on a combination of factors, for example the relative surface brightness of the main object to that of the contaminants, their distance on the sky and on the presence of spectral features. Although some of these quantities can be calculated by the pipeline it is useful to provide an additional comprehensive human assessment of the degree of contamination. After significant experiments we decided to divide the spectra in three classes of

contamination mild, moderate and severe. Roughly speaking, the three categories refer to spectra where the area of the detector with contamination sufficient to affect the target spectrum is considered to be respectively $<10\%$, $10\%–40\%$ $>40\%$ although the assessment takes into account all the factors listed above. As shown in Figure 7, approximately 40% of all spectra have mild contamination. However, thanks to two-PA strategy, there is at least one clean spectrum for more than 60% of all the objects in the catalog.

3. Flag and identify strong emission lines and the presence of a continuum. During the inspection of the spectra a box is ticked to denote the detection of a continuum, and the wavelengths of identified lines are marked. This information can be used in the next step of determining redshifts, allowing one, for example, to visually inspect only the spectra where continuum or emission lines are present.
4. Note additional features. The user can also provide additional comments, or flag the object as being a star or defect etc.

In practice, in order to provide some safeguard against the inevitable subjectivity associated with visual inspection, each cluster catalog is inspected by at least two team members. For MACS J0717.5+3745 co-authors T.T. and B.V. visually classified the entire data set of 1151 objects down to magnitude $H_{AB} < 24$ (F140W). This deep classification was conducted on the first cluster for exploration purposes. For the remaining clusters full visual inspection will be limited to $H_{AB} = 23$, plus a search for emission lines in the fainter objects. For reference, the distribution of photometric redshifts, taken from the CLASH catalog, of the parent sample, and the sample limited to $H < 23$ is shown in Figure 8. The two inspection catalogs were merged by averaging numeric flags, i.e., if one inspector assigned mild (0) contamination and the other assigned severe (1) contamination, the entry in the combined catalog is 0.5.

We caution that the inspection performed by the team is of general purpose, and even though it should provide a useful guidance for anyone interested in the GLASS data, it may not suffice for very specific applications. For example, a dedicated

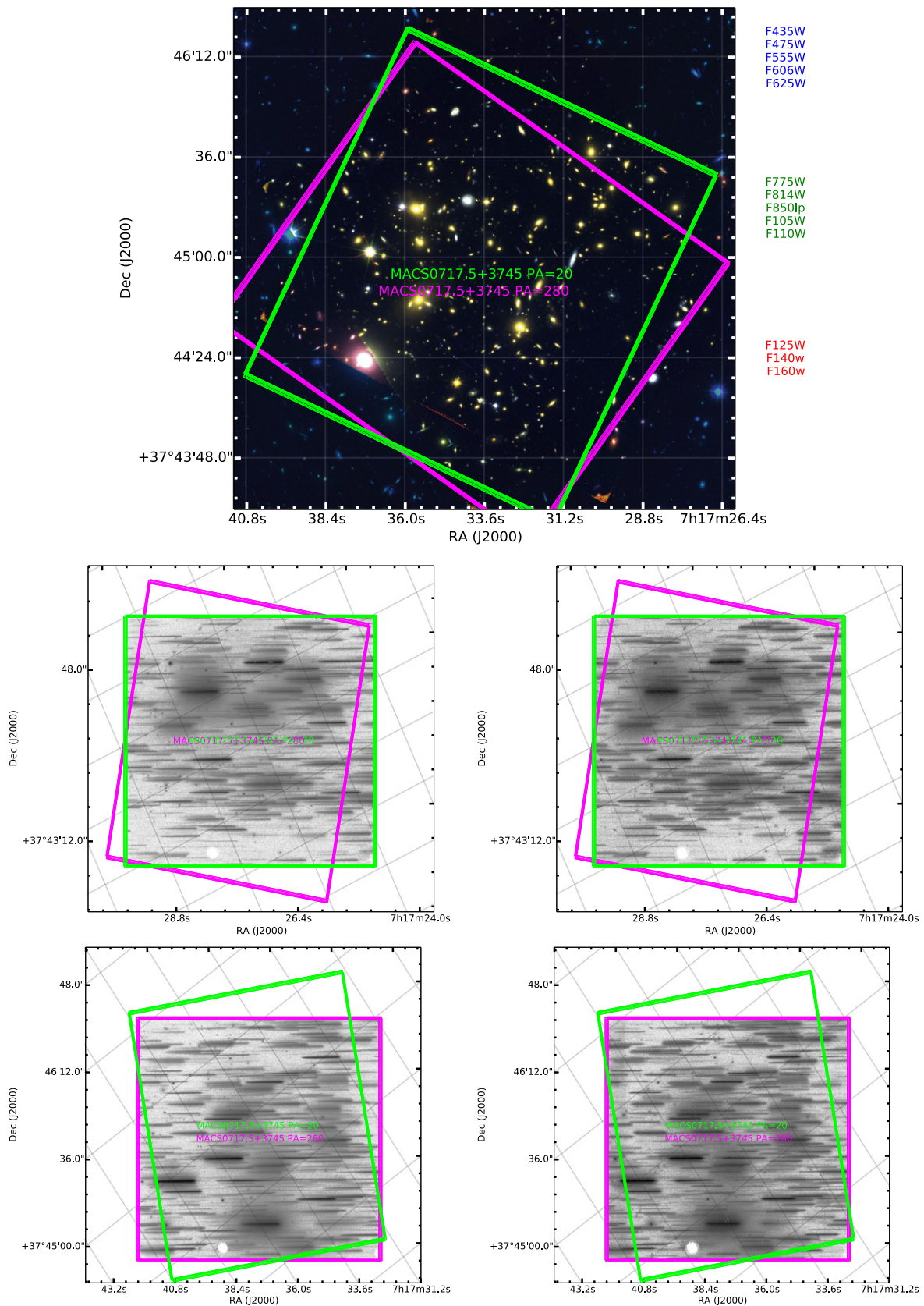


Figure 6. MACS J0717.5+3745 GLASS fields of view. The color composite image (top) is based on the CLASH imaging with blue, green, and red channels as noted on the right. The four bottom panels show the final interlaced sky-subtracted G102 (left) and G141(right) grism mosaics at the position angle 20 (top; green polygons) and 280 (bottom; magenta polygons) degrees. The individual spectra are extracted from these mosaics based on the extent of the corresponding object in the direct image mosaics (not shown here).

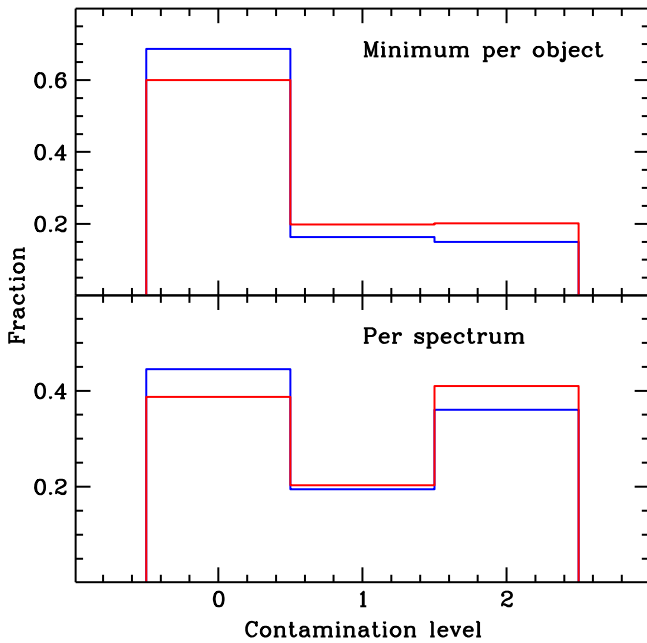


Figure 7. Contamination statistics for the MACS J0717.5+3745 catalog. The distribution of contamination levels (0 = mild, 1 = moderate, 2 = severe) assigned by one classifier is shown by object and by spectrum, for the G102 (blue) and G141 (red) grisms. Approximately 40% of the spectra suffer from mild contamination and are therefore “clean.” However, thanks to the two position angle observing strategy more than 60% of the objects have at least one clean spectrum.

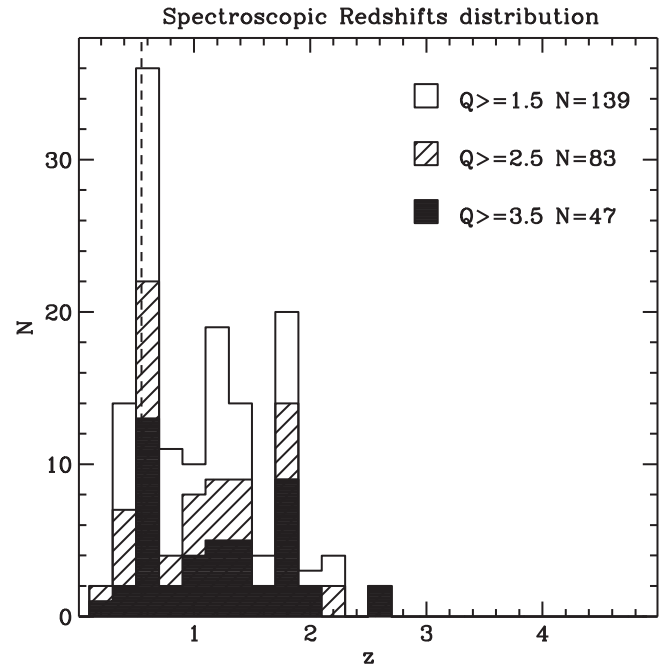


Figure 9. Redshift distribution of emission line sources identified from the WFC3 GLASS spectra in the field of MACS J0717.5+3745. Note the peak at the cluster redshift $z = 0.548$ (vertical dashed line). Stars are not included in the histogram and tally.

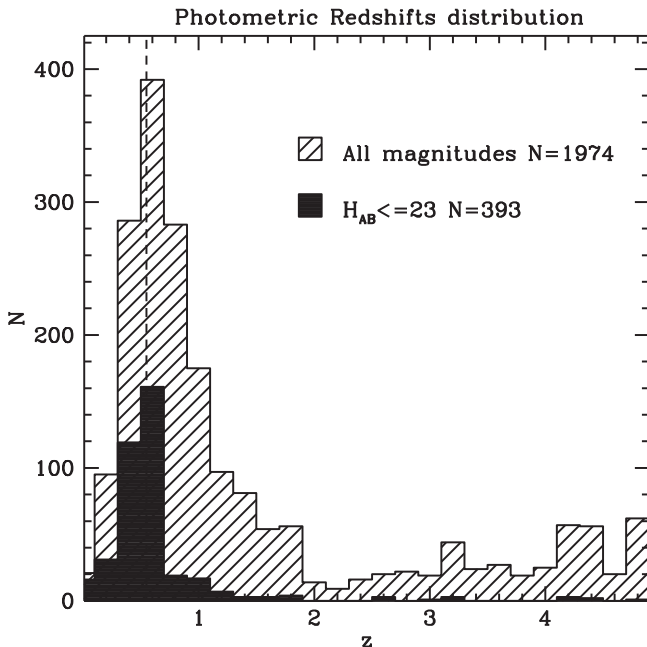


Figure 8. Distribution of photometric redshifts for the all the sources in the CLASH catalog of MACS J0717.5+3745. The cluster redshift ($z = 0.548$) is indicated by a vertical dashed line.

re-inspection of photometrically selected high-redshift galaxies was carried out by the team while looking for faint Ly α emission (Schmidt et al. 2015).

5.2. Redshift Determination

Redshift determination is performed in two steps. In the first step, templates are fit to each of the four available grism spectra independently (G102 and G141 at two PAs each) to determine a posterior distribution function for the redshift. If available, photometric redshift distributions can be used as input priors to the grism fits in order to reduce computational time. Quite frequently, the information content of the four exposures is rather uneven, for example, because some of the spectra are strongly contaminated, or maybe because emission lines fall in only one of the two grisms (G102 or G141) and no continuum is present in the other. Rather than blindly combining the four pdfs, the team decided to undergo a step of visual inspection using the dedicated publicly available GLASS inspection GUI for redshifts (GIGz; described in the Appendix). With the help of GIGz the user can flag which grism fits are reliable or alternatively enter a redshift by hand if the redshift is misidentified by the automatic procedure. As described in the Appendix GIGz is fully interactive. This is carried out for all galaxies down to a magnitude limit of $H < 23$, as well for additional samples as described in the next two sections.

Using GIGz we assigned a quality flag to the redshift according to the following scheme (4 = secure; 3 = probable; 2 = possible; 1 = tentative, but likely an artifact; 0 = no- z). These quality criteria take into account the signal-to-noise ratio of the detection, the possibility that the line is a contaminant, and the identification of the feature with a specific emission line. For example, $Q = 4$ indicates multiple emission have been detected with high signal-to-noise ratio and thus there is no doubt of the redshift identification; $Q = 3$ indicates that either a single strong emission line is robustly detected and the redshift identification is supported by the photometric redshift, or that more than one feature is marginally detected; $Q = 2$ indicates a single line detection of marginal quality; $Q = 1$ indicates that

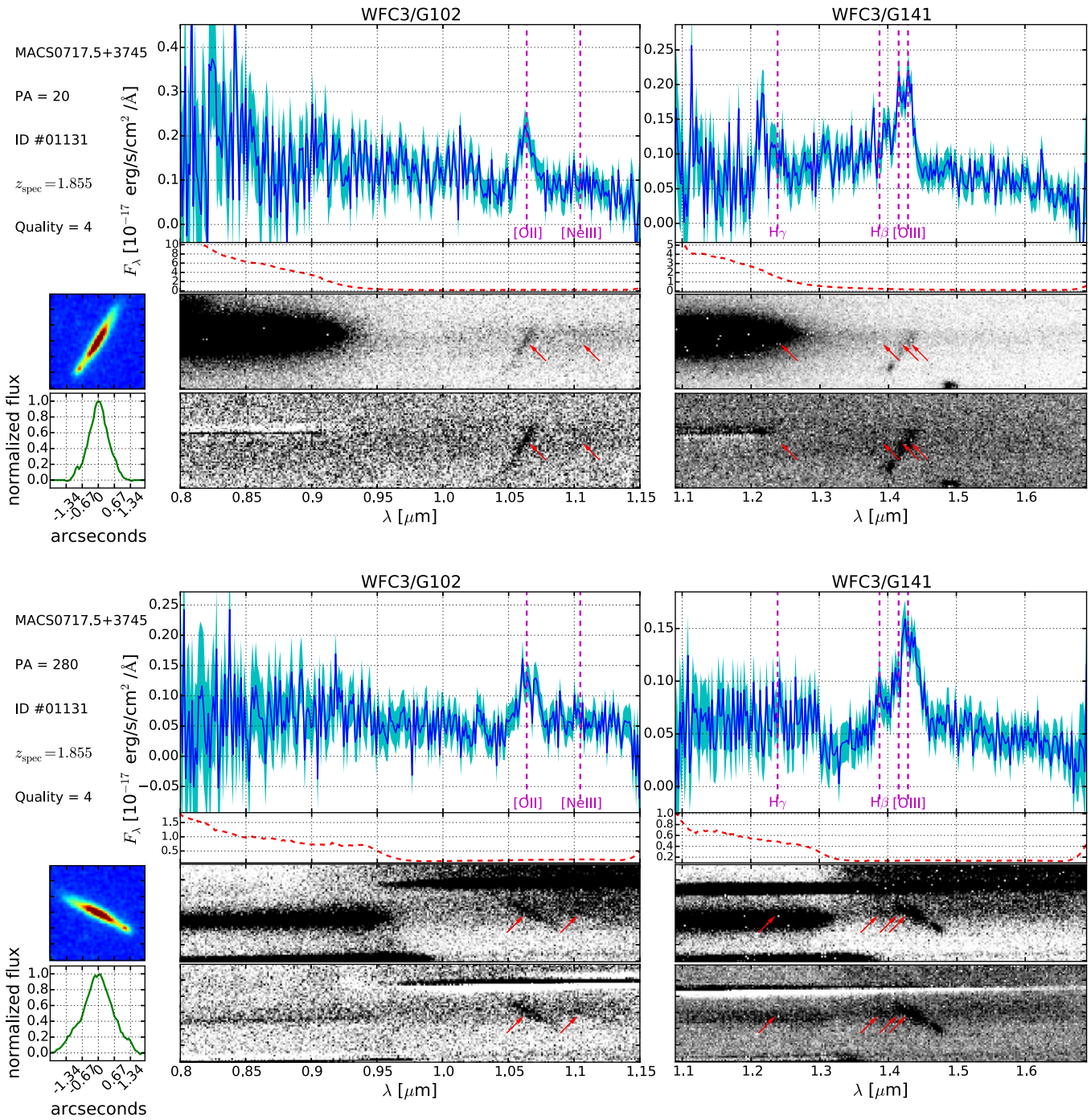


Figure 10. Spectra for GLASS ID #1131 (also known as arc 4.1). In each sub-figure, the two panels on top show the one-dimensional spectra, where the observed flux and contamination model are denoted by blue solid and red dashed lines, respectively. The cyan shaded region represents the noise level. For the four panels directly underneath, the middle two display the interlaced two-dimensional spectra, whereas the bottom two have contamination subtracted. In the one- and two-dimensional spectra, the identified emission lines are denoted by vertical dashed lines in magenta and arrows in red, respectively. The two panels on the left show the two-dimensional postage stamp created from the HFF co-adds through drizzling (top) and the one-dimensional collapsed image (bottom). Note that these two panels share the same x-axis along the grism dispersion direction. Some ancillary information is also shown in the upper left corner in each sub-figure, including the redshift quality flag Q.

there is something but it is most likely an artifact. We also ticked boxes to indicate secure identification of some of the more common and stronger lines. In some cases there is ambiguity about the identification of a single emission lines. Those instances are marked during the inspection process. This procedure is carried out independently by each inspector and then their outputs are combined.

5.3. Search for Emission Lines in Faint Sources

In addition to the systematic visual inspection of the magnitude-limited catalog, a search for emission lines was carried out by three of the authors (T.T., K.B.S., B.V.), based on visual inspection of all the jpegs of the two-dimensional spectra of objects with continuum fainter than the $H < 23$ limit. For each object, the authors inspected the spectra, the

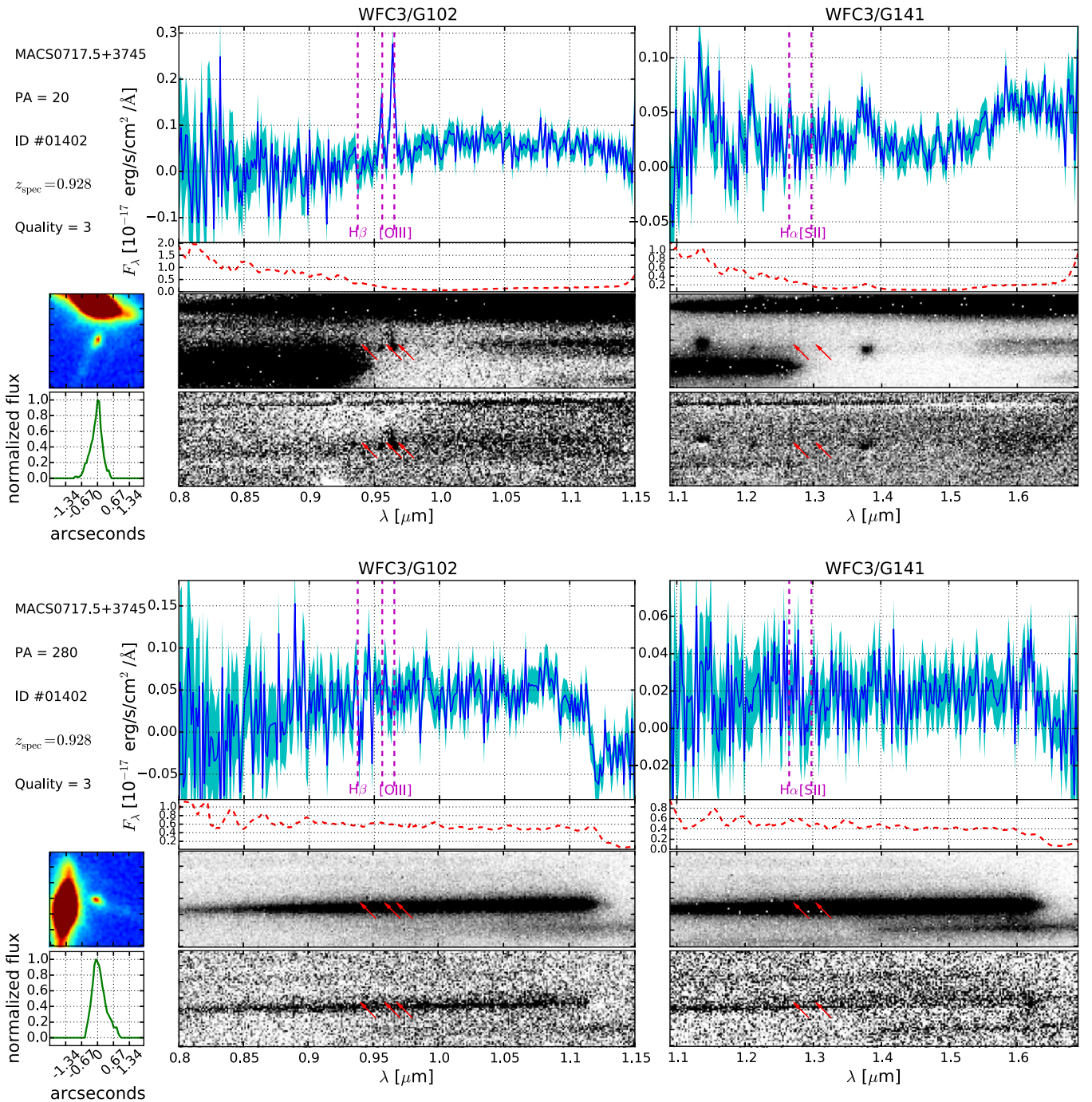


Figure 12. As Figure 10 for GLASS ID 1402 (arc 12.1). The data at PA = 280 suffer from strong contamination from the nearby galaxy.

authors (T.T. and X.W.). We confirm the redshifts of several previously known systems, including from our own GLASS survey (paper 0) and those measured by other teams (Ma et al. 2008; Limousin et al. 2012; Ebeling et al. 2014), and measure three new redshifts. One of them (image 5.1, GLASS ID = 1108, $z = 0.928$) is classified as probable and differs substantially from the value $z = 4.3$ assumed by Diego et al. (2014). Two of the redshifts are tentative and should not be used until further confirmation (29.2, GLASS ID = 378 $z = 1.73$; 55.2, GLASS ID = 82, $z = 0.47$, which would be in the foreground if confirmed).

5.5. Properties of the Spectroscopic Sample and Example Spectra

A histogram of redshifts based on emission lines detected in the WFC3 grism spectra is shown in Figure 9. Besides a clear peak associated with the cluster redshift, the distribution covers a broad range in redshifts. Some examples of spectra are shown in Figures 10–15. We show one example each of quality 4, 3, and 2 redshifts, including multiply image candidates when possible. The examples are meant to illustrate the diversity of the data, including incomplete data sets, arising from edge effects or strong contamination.

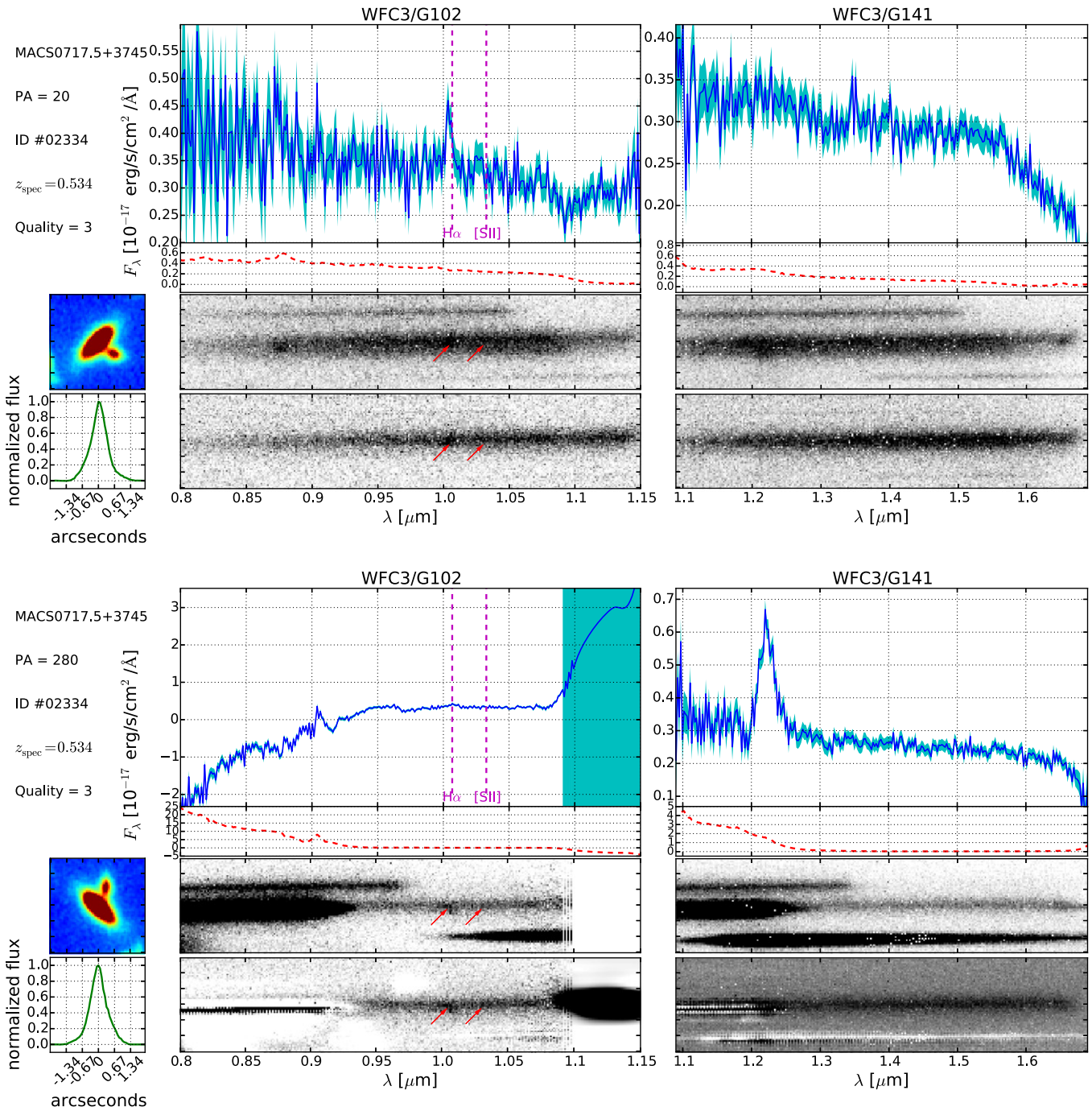


Figure 13. As Figure 10 for cluster member GLASS ID 2334.

6. PUBLICLY AVAILABLE DATA AND TOOLS

6.1. Release Plan

For each cluster we plan three releases.

1. Release 1. WFC3 images and spectra. In order to provide the most useful match to the photometry provided by the CLASH collaboration for the first GLASS, the spectra are extracted based on photometric catalogs generated by running SEXtractor (Bertin & Arnouts 1996) on the GLASS IR detection image using the same parameters as those adopted by CLASH (D. Coe 2015, private communication; available at the GLASS website). All

the spectra are visually inspected to magnitude $F_{140W} < 23AB$. The structure of the data and naming of the files is identical to that produced for 3D-HST, with the addition of stack files that combine the two PAs into a single spectrum. More details are available from the 3D-HST paper and at the HST archive. In addition, a catalog is provided in electronic form. The first few entries are shown in Table 3 for guidance.

2. Release 2. ACS images and spectra in the parallel fields. The spectra are extracted based on catalogs generated from the GLASS ACS images themselves. Visual inspection will be performed to a magnitude limit to be defined. The data and catalog structure will be as similar

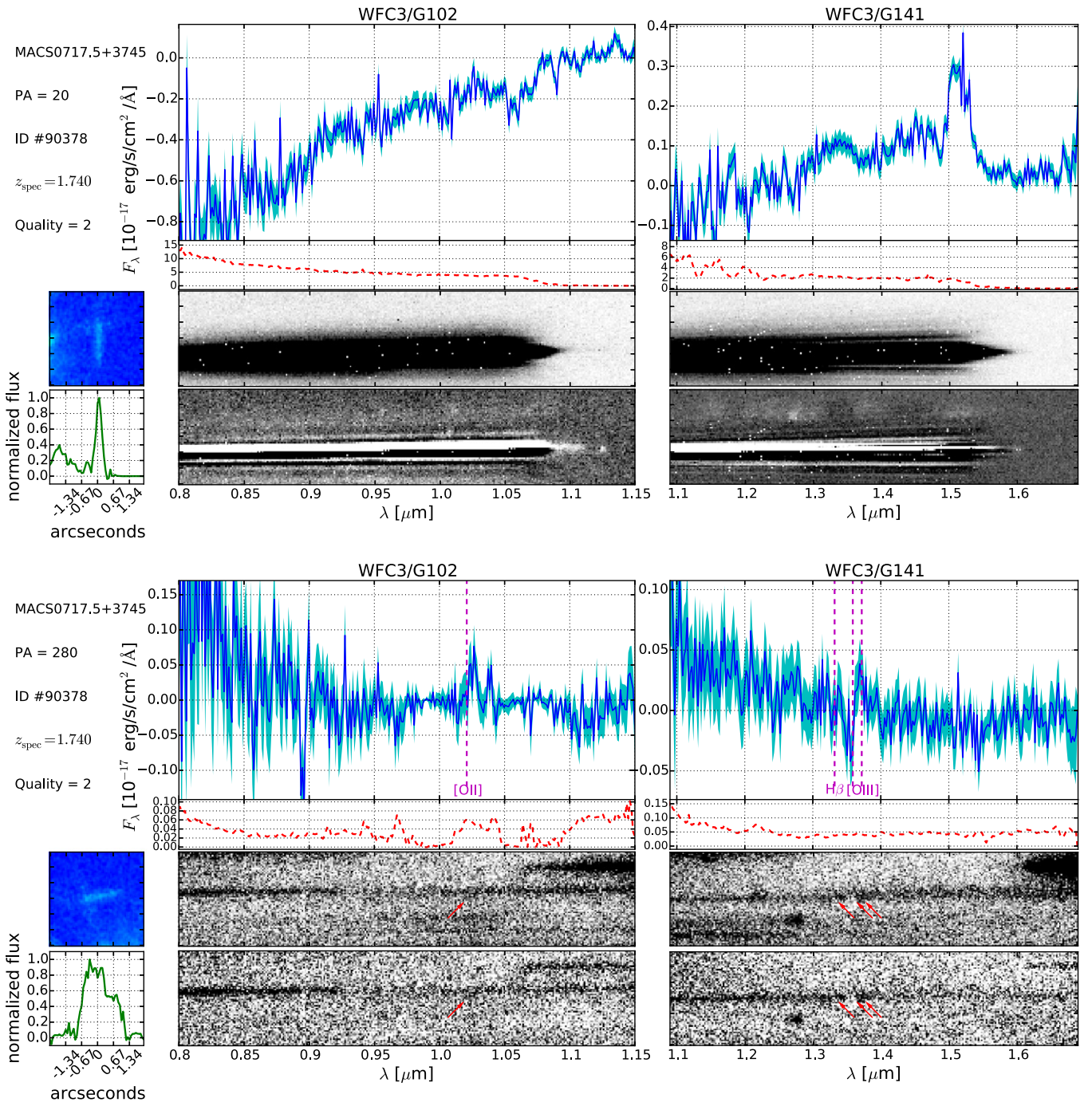


Figure 14. As Figure 10 for GLASS ID 90378 (arc 29.2). Data at PA = 20 suffer from strong contamination from a nearby star. The data at PA = 280 show low signal-to-noise ratio emission lines, thus justifying quality flag $Q = 2$.

as possible to that of the WFC3 data and will be described in a future publication.

3. Release 3. WFC3 and ACS spectra. The spectra are extracted based on catalogs generated from the final images of the clusters, after the completion of the HFF campaigns. Spectra of newly identified objects are visually inspected and redshifts are recalculated based on updated photometric redshifts.

Barring the unexpected, the first release is scheduled to happen within approximately one year from the acquisition of the data (see Table 1; release will start after this paper is

accepted). The second release is tentatively scheduled to follow by approximately 6–12 months. The third release will depend on availability of other data sets and availability of funds. The publicly released data will be available through the Mikulski Archive for Space Telescopes (MAST) at URL <https://archive.stsci.edu/prepds/glass/>.

7. SUMMARY

This paper provides an overview of the GLASS survey. After reviewing the scientific motivations that drove the survey design, the paper describes the data and data processing steps.

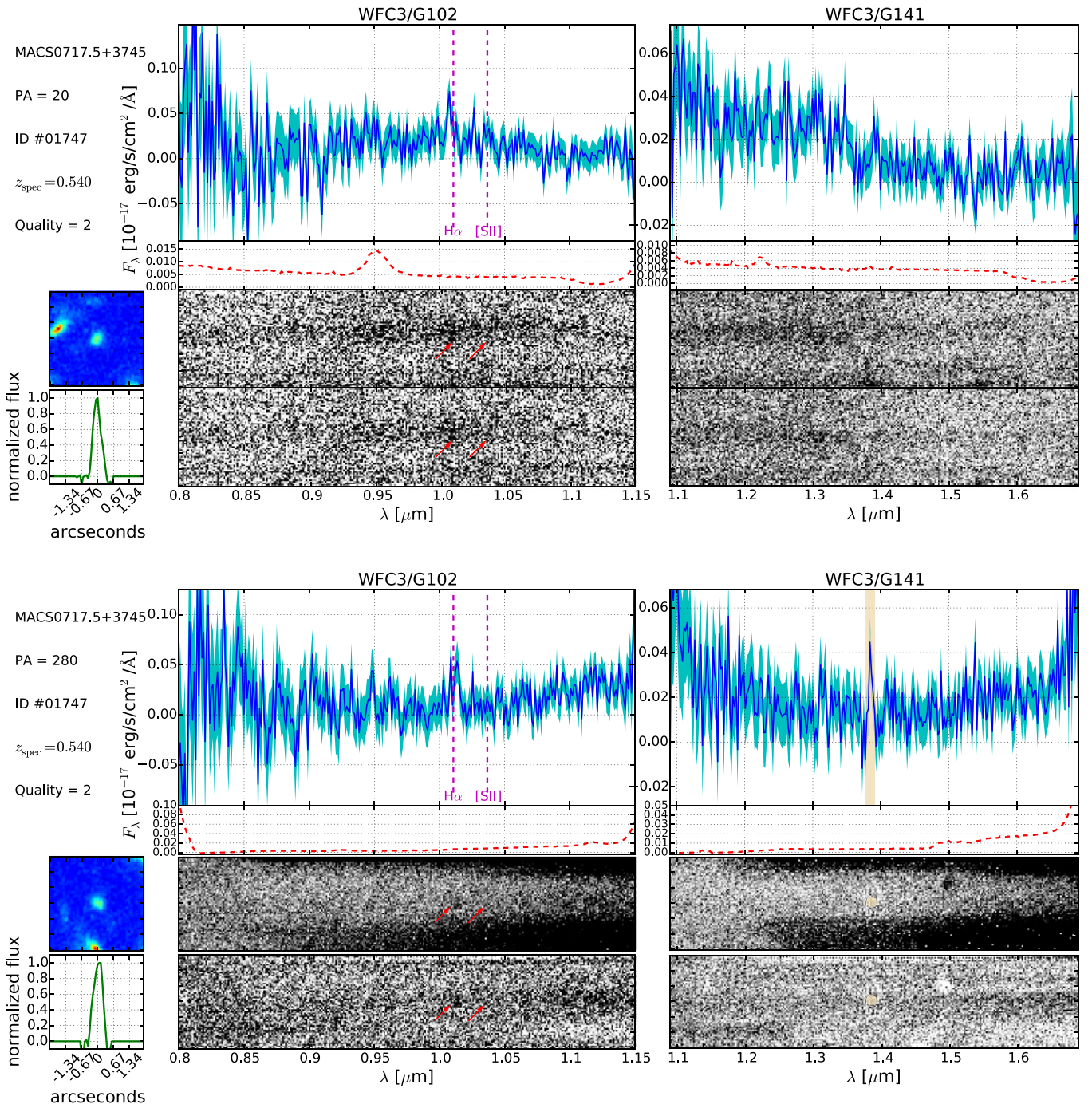


Figure 15. As Figure 10 for cluster member GLASS ID 1747. A low signal-to-noise ratio emission line is detected at both PA, and tentatively identified as Balmer H α at the cluster redshift.

We use MACS J0717.5+3745, the first cluster observed by GLASS (and part of the HFF campaign), to illustrate the data set. The main results of this paper can be summarized as follows.

1. The line flux sensitivity of GLASS reaches $\approx 4\text{--}5 \times 10^{-18} \text{ erg s}^{-1} \text{ cm}^{-2}$ (1σ) for clean spectra of compact sources in the most sensitive wavelength range, for each of the two position angles. The observing strategy, consisting of two orthogonal position angles, is effective in reducing the effects of foreground contamination. Whereas $\sim 40\%$ of the individual spectra are
- classified as suffering from mild contamination (i.e., being virtually clean), more than 60% of the objects are observed as clean at at least one position angle. For those objects for which clean spectra are available at both position angles, the sensitivity reaches $\approx 3 \times 10^{-18} \text{ erg s}^{-1} \text{ cm}^{-2}$ (1σ).
2. The first data release for cluster MACS J0717.5+3745 is complete, and high level data products made publicly available. Spectra for 1151 galaxies down to magnitude $H_{\text{AB}} < 24$ (F140W) have been visually inspected by members of our team to ensure quality control.

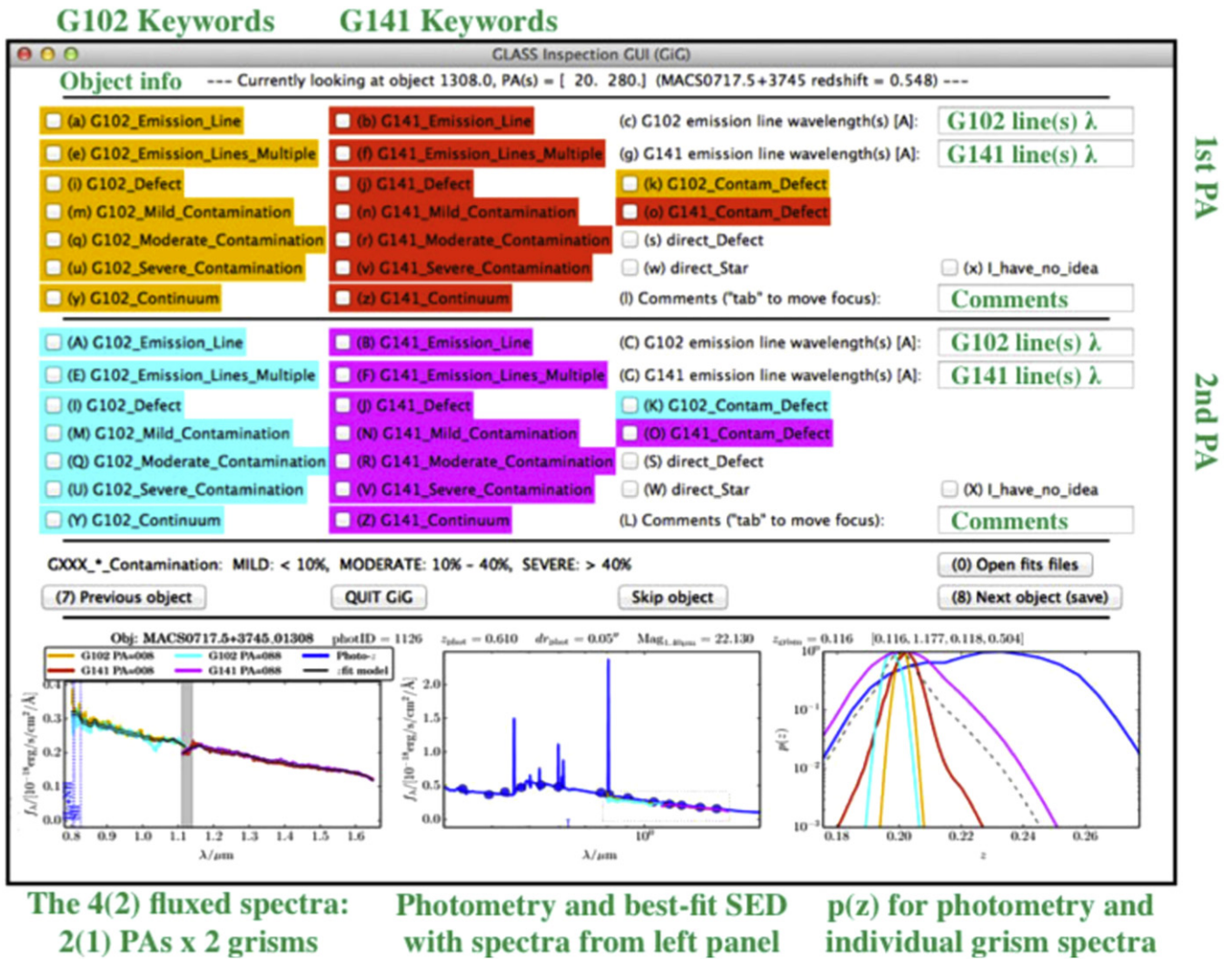


Figure 16. Overview of the GiG interface. The green text comments on the individual parts of the GUI. The software is publicly available for download at <https://github.com/kasperschmidt/GLASSinspectionGUIs>.

3. A visual search for emission lines has been carried out through the entire data set, including galaxies fainter than the inspection limit. In total, we measure emission line redshifts for 139 extragalactic sources. The redshift catalog is made public in electronic format as part of the first data release.
4. A dedicated search for redshift of candidate multiple imaged sources reveals three new redshifts, as well as confirming several previously known systems.
5. In addition to the high-level data products we make available two Graphic User Interfaces (GiG and GiGz) which allow for efficient browsing of the data set, and interactive redshift determination. The GUIs are described in the [Appendix](#).

Support for GLASS (*HST*-GO-13459) was provided by NASA through a grant from the Space Telescope Science Institute, which is operated by the Association of Universities for Research in Astronomy, Inc., under NASA contract NAS 5-26555. We are very grateful to the staff of the Space Telescope for their assistance in planning, scheduling and executing the observations, and in setting up the GLASS public release website. We thank the referee for helpful suggestions

that improved the paper. T.T. gratefully acknowledges the hospitality of the American Academy in Rome and of the Observatorio di Monteporzio Catone, where parts of this manuscript were written. B.V. acknowledges the support from the World Premier International Research Center Initiative (WPI), MEXT, Japan and the Kakenhi Grant-in-Aid for Young Scientists (B) (26870140) from the Japan Society for the Promotion of Science (JSPS).

APPENDIX THE GLASS INSPECTION GUI (GiG)

In this appendix we describe the GiG and the GLASS inspection GUI for redshifts (GiGz) v1.0, released as part of the first public data release from GLASS described in this paper. This Python-based software provides a convenient and efficient way of inspecting and browsing the GLASS data products and is made publicly available for download at <https://github.com/kasperschmidt/GLASSinspectionGUIs>. A more detailed and continuously updated description of the software package can be found in the document *GiG_README.pdf* which is also available at <https://github.com/kasperschmidt/GLASSinspectionGUIs>.

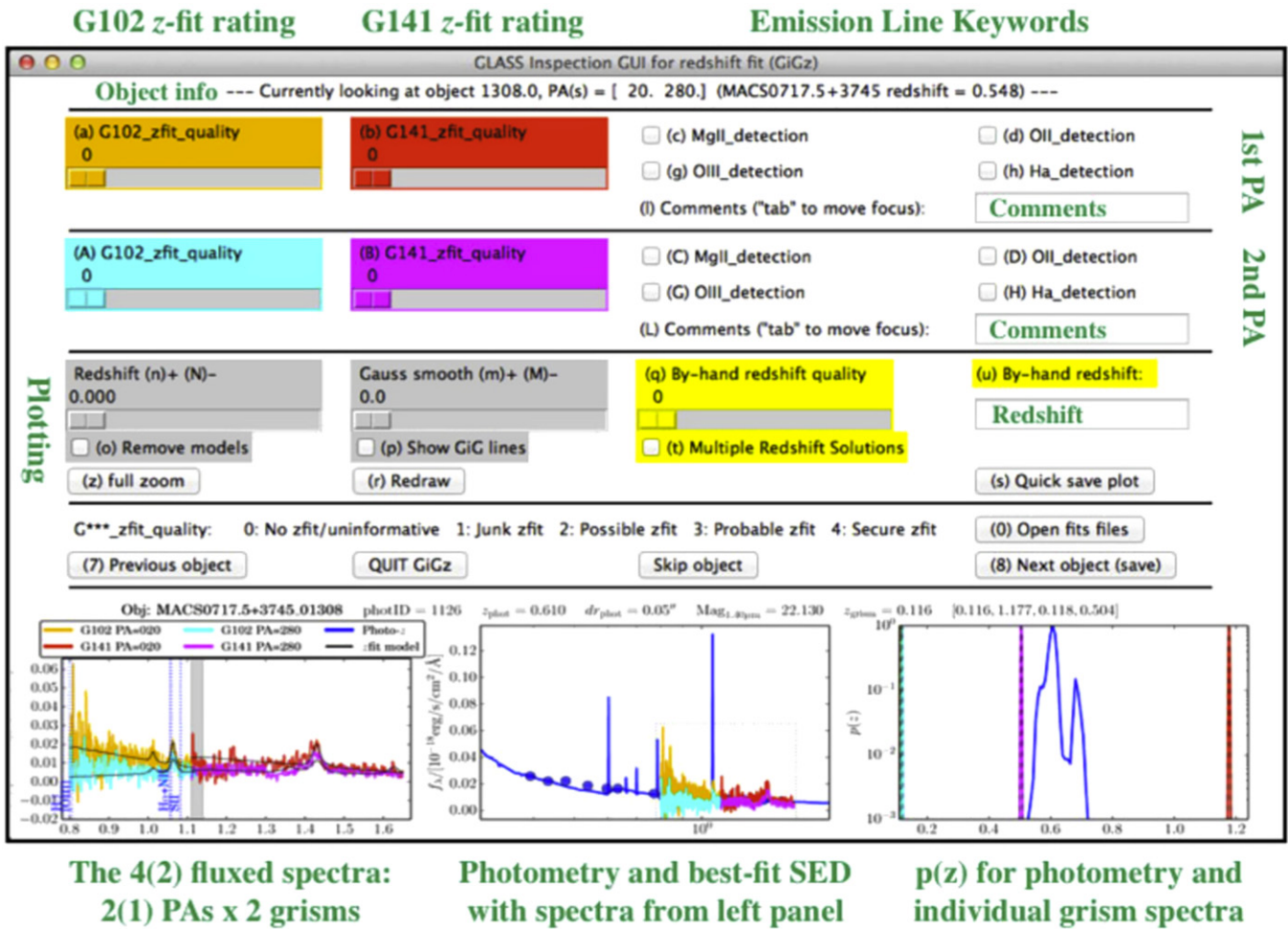


Figure 17. Overview of the GiGz interface. The green text comments on the individual parts of the GUI. The software is publicly available for download at <https://github.com/kasperschmidt/GLASSinspectionGUIs>.

A.1. The GLASS Inspection GUI

GiG is designed to inspect and browse the main products from the data reduction pipeline described in Section 4.2. Overview and descriptions of the products are available from the 3D-*HST* papers and the *HST* MAST archive. In brief, they include the extracted two-dimensional spectra, stacks of the spectra at the two separate position angles in 2D, extracted one-dimensional spectra, and various diagnostic plots. GiG (and GiGz described below) are self-contained in the Python script `visualinspection.py` and only depend on standard publicly available python packages (see <https://github.com/kasperschmidt/GLASSinspectionGUIs/blob/master/README.pdf>) for details. A general overview of the interface of GiG v1.0 is shown in Figure 16. GiG allows the user to quickly visualize all data products, including direct inspection of two-dimensional fits files via interfacing with ds9. In addition to visualization, GiG allows the user to rate the contamination of the individual spectra at the two GLASS PAs, indicate the presence of a continuum, mark defects in the spectra or contamination models and mark emission lines including noting the redshift at which the lines were identified.

The contamination levels are rated as mild, moderate, or severe corresponding to roughly <10%, 10%–40% and >40 flux contamination of the central region where the spectral trace of the object displayed is expected to be. As this rating is

somewhat subjective an automatically generated estimated of the level of flux in the pixels “belong” to the spectrum is stored in the GiG output file. This contamination level is defined as the fraction of pixels in the fits-extension of the extracted 2D spectra containing the contamination model (masked by the object model extension) with $>10^{-3} \text{ e s}^{-1} \text{ pixel}^{-1}$.

Apart from the manually set keywords and the automatic contamination estimate, the spectral coverage of each spectrum is also estimated and stored automatically in the output file.

A.2. The GLASS Inspection GUI for Redshifts

GiGz is developed for general inspection of the extracted 1D spectra, the inspection of the redshift fits generated as described by (Brammer et al. 2012), and for manual redshift fitting of any detected emission lines. The default GUI window shown for GiGz v1.0 in Figure 17 enables quality assessment of the redshift fits and flagging of particular lines identified for easy identification of, e.g., [O III] emitters in the data set. GiGz also includes an interactive plotting interface which can be controlled from the main window. This enables a convenient way of plotting and inspecting the extracted 1D spectra, the redshift models, and any emission lines identified in the GiG inspection. Two-dimensional fits files of the spectra can also be inspected through GiG via a ds9 interface.

REFERENCES

- Amorín, R. O., Pérez-Montero, E., & Vilchez, J. M. 2010, *ApJL*, 715, L128
- Andrews, B. H., & Martini, P. 2013, *ApJ*, 765, 140
- Atek, H., Malkan, M., McCarthy, P., et al. 2010, *ApJ*, 723, 104
- Atek, H., Siana, B., Scarlata, C., et al. 2011, *ApJ*, 743, 121
- Baldwin, J. A., Phillips, M. M., & Terlevich, R. 1981, *PASP*, 93, 5
- Bayliss, M. B., Rigby, J. R., Sharon, K., et al. 2014, *ApJ*, 790, 144
- Becker, G. D., Bolton, J. S., Madau, P., et al. 2015, *MNRAS*, 447, 3402
- Belli, S., Jones, T., Ellis, R. S., & Richard, J. 2013, *ApJ*, 772, 141
- Bennett, C. L., Larson, D., Weiland, J. L., et al. 2013, *ApJS*, 208, 20
- Bertin, E., & Arnouts, S. 1996, *A&AS*, 117, 393
- Bolton, A. S., & Burles, S. 2003, *ApJ*, 592, 17
- Bouwens, R. J., Illingworth, G. D., Oesch, P. A., et al. 2014, arXiv:1403.4295
- Bradač, M., Schneider, P., Lombardi, M., & Erben, T. 2005, *A&A*, 437, 39
- Bradač, M., Schrabback, T., Erben, T., et al. 2008, *ApJ*, 681, 187
- Bradač, M., Treu, T., Applegate, D., et al. 2009, *ApJ*, 706, 1201
- Bradley, L. D., Trenti, M., Oesch, P. A., et al. 2012, *ApJ*, 760, 108
- Brammer, G., Kelly, P., Rodney, S., Schmidt, K. B., & Treu, T. 2014a, *ATel*, 5728, 1
- Brammer, G. B., Pirzkal, N., McCullough, P. R., & MacKenty, J. W. 2014b, *STScI IRS*
- Brammer, G. B., van Dokkum, P. G., Franx, M., et al. 2012, *ApJS*, 200, 13
- Bresolin, F., Kennicutt, R. C., & Ryan-Weber, E. 2012, *ApJ*, 750, 122
- Butcher, H., & Oemler, A., Jr. 1984, *ApJ*, 285, 426
- Choudhury, T. R., Puchwein, E., Hahnelt, M. G., & Bolton, J. S. 2014, arXiv:1412.4790
- Clément, B., Cuby, J.-G., Courbin, F., et al. 2012, *A&A*, 538, A66
- Coe, D., Bradley, L., & Zitrin, A. 2014, arXiv:1405.0011
- Colbert, J. W., Teplitz, H., Atek, H., et al. 2013, *ApJ*, 779, 34
- Cooper, M. C., Newman, J. A., Weiner, B. J., et al. 2008, *MNRAS*, 383, 1058
- Council, N. R. 2010, *New Worlds, New Horizons in Astronomy and Astrophysics* (Washington, DC: The National Academies Press)
- Diego, J. M., Broadhurst, T., Zitrin, A., et al. 2014, arXiv:1410.7019
- Dijkstra, M. 2014, *PASA*, 31, 40
- Dijkstra, M., Mesinger, A., & Wyithe, J. S. B. 2011, *MNRAS*, 414, 2139
- Dressler, A., Oemler, A., Jr., Poggianti, B. M., et al. 2013, *ApJ*, 770, 62
- Dressler, A., Smail, I., Poggianti, B. M., et al. 1999, *ApJS*, 122, 51
- Ebeling, H., Ma, C.-J., & Barrett, E. 2014, *ApJS*, 211, 21
- Ellis, R. S., McLure, R. J., Dunlop, J. S., et al. 2013, *ApJL*, 763, L7
- Ferguson, H. C., Dickinson, M., & Williams, R. 2000, *ARA&A*, 38, 667
- Finlator, K., & Davé, R. 2008, *MNRAS*, 385, 2181
- Finn, R. A., Zaritsky, D., McCarthy, D. W., Jr., et al. 2005, *ApJ*, 630, 206
- Fontana, A., Vanzella, E., Pentericci, L., et al. 2010, *ApJL*, 725, L205
- Fumagalli, M., Patel, S. G., Franx, M., et al. 2012, *ApJL*, 757, L22
- Giallongo, E., Grazian, A., Fiore, F., et al. 2015, arXiv:1502.02562
- Giallisco, M., Ferguson, H. C., Koekemoer, A. M., et al. 2004, *ApJ*, 600, L93
- Gibson, B. K., Pilkington, K., Brook, C. B., Stinson, G. S., & Bailin, J. 2013, *A&A*, 554, A47
- Gonzaga, S., Hack, W., Fruchter, A., & Mack, J. 2012, *The DrizzlePac Handbook, HST Data Handbook*
- Guaita, L., Melinder, J., Hayes, M., et al. 2015, *A&A*, 576, A51
- Henry, A., Scarlata, C., Dominguez, A., et al. 2013, *ApJL*, 776, L27
- Holz, D. E. 2001, *ApJL*, 556, L71
- Jensen, H., Laursen, P., Møller, G., et al. 2013, *MNRAS*, 428, 1366
- Jones, T., Ellis, R., Jullo, E., & Richard, J. 2010, *ApJL*, 725, L176
- Jones, T., Ellis, R. S., Richard, J., & Jullo, E. 2013a, *ApJ*, 765, 48
- Jones, T., Wang, X., Schmidt, K. B., et al. 2015, *AJ*, 149, 107
- Jones, T. A., Ellis, R. S., Schenker, M. A., & Stark, D. P. 2013b, *ApJ*, 779, 52
- Kashikawa, N., Shimasaku, K., Malkan, M. A., et al. 2006, *ApJ*, 648, 7
- Kelly, P. L., Rodney, S. A., Treu, T., et al. 2015, *Sci*, 347, 1123
- Kennicutt, R. C. 1998, *ARA&A*, 36, 189
- Kewley, L. J., Maier, C., Yabe, K., et al. 2013, *ApJL*, 774, L10
- Kodama, T., Balogh, M. L., Smail, I., Bower, R. G., & Nakata, F. 2004, *MNRAS*, 354, 1103
- Koekemoer, A. M., Faber, S. M., Ferguson, H. C., et al. 2011, *ApJS*, 197, 36
- Koekemoer, A. M., Fruchter, A. S., Hook, R. N., & Hack, W. 2003, in *The 2002 HST Calibration Workshop: Hubble After the Installation of the ACS and the NICMOS Cooling System*, 337
- Koopmann, R. A., & Kenney, J. D. P. 2004, *ApJ*, 613, 866
- Koyama, Y., Kodama, T., Nakata, F., Shimasaku, K., & Okamura, S. 2011, *ApJ*, 734, 66
- Koyama, Y., Kodama, T., Tadaki, K.-i., et al. 2013, *MNRAS*, 428, 1551
- Kümmel, M., Kuntschner, H., Walsh, J. R., & Bushouse, H. 2011, *ST-ECF Instrument Science Rep. WFC3-2011-01*, 1
- Lamareille, F. 2010, *A&A*, 509, A53
- Lilly, S. J., Fevre, O. L., Hammer, F., & Crampton, D. 1996, *ApJL*, 460, L1
- Limousin, M., Ebeling, H., Richard, J., et al. 2012, *A&A*, 544, 71
- Ma, C.-J., Ebeling, H., Donovan, D., & Barrett, E. 2008, *ApJ*, 684, 160
- Madau, P., & Dickinson, M. 2014, *ARA&A*, 52, 415
- Madau, P., Ferguson, H. C., Dickinson, M. E., et al. 1996, *MNRAS*, 283, 1388
- Madau, P., Rees, M. J., Volonteri, M., Haardt, F., & Oh, S. P. 2004, *ApJ*, 604, 484
- Mannucci, F., Cresci, G., Maiolino, R., Marconi, A., & Gnerucci, A. 2010, *MNRAS*, 408, 2115
- Mantz, A., Allen, S. W., Ebeling, H., Rapetti, D., & Drica-Wagner, A. 2010, *MNRAS*, 406, 1773
- Mason, C., Trenti, M., & Treu, T. 2015, *ApJ*, submitted (arXiv:1508.01204)
- Masters, D., McCarthy, P., Siana, B., et al. 2014, *ApJ*, 785, 153
- McCarthy, P. J., Yan, L., Freudling, W., et al. 1999, *ApJ*, 520, 548
- McLean, I. S., Steidel, C. C., Epps, H. W., et al. 2012, *Proc. SPIE*, 8446, 84460J
- McQuinn, M., Hernquist, L., Zaldarriaga, M., & Dutta, S. 2007, *MNRAS*, 381, 75
- Mesinger, A., Aykutaalp, A., Vanzella, E., et al. 2015, *MNRAS*, 446, 566
- Mesinger, A., McQuinn, M., & Spergel, D. N. 2012, *MNRAS*, 422, 1403
- Meylan, G., Jetzer, P., North, P., et al. 2006, in *Saas-Fee Advanced Course 33: Gravitational Lensing: Strong, Weak and Micro* (Berlin: Springer)
- Morris, A. M., Kocevski, D. D., Trump, J. R., et al. 2015, *AJ*, 149, 178
- Moustakas, J., Kennicutt, R. C., Jr., & Tremonti, C. A. 2006, *ApJ*, 642, 775
- Muzzin, A., Wilson, G., Yee, H. K. C., et al. 2012, *ApJ*, 746, 188
- Nelson, E. J., van Dokkum, P. G., Brammer, G., et al. 2012, *ApJL*, 747, L28
- Newman, A. B., Ellis, R. S., Andreon, S., et al. 2014, *ApJ*, 788, 51
- Nordin, J., Rubin, D., Richard, J., et al. 2014, *MNRAS*, 440, 2742
- Oemler, A., Jr., Dressler, A., Gladders, M. G., et al. 2013, *ApJ*, 770, 63
- Oesch, P. A., Bouwens, R. J., Illingworth, G. D., et al. 2013, *ApJ*, 773, 75
- Ono, Y., Ouchi, M., Mobasher, B., et al. 2012, *ApJ*, 744, 83
- Ouchi, M., Mobasher, B., Shimasaku, K., et al. 2009, *ApJ*, 706, 1136
- Patel, B., McCully, C., Jha, S. W., et al. 2014, *ApJ*, 786, 9
- Peng, Y.-j., Lilly, S. J., Kovač, K., et al. 2010, *ApJ*, 721, 193
- Pentericci, L., Fontana, A., Vanzella, E., et al. 2011, *ApJ*, 743, 132
- Pentericci, L., Vanzella, E., Fontana, A., et al. 2014, *ApJ*, 793, 113
- Pilkington, K., Few, C. G., Gibson, B. K., et al. 2012, *A&A*, 540, A56
- Pirzkal, N., Rothberg, B., Ly, C., et al. 2013, *ApJ*, 772, 48
- Planck Collaboration 2015, arXiv:1502.01589
- Poggianti, B. M., Smail, I., Dressler, A., et al. 1999, *ApJ*, 518, 576
- Postman, M., Coe, D., Benítez, N., et al. 2012, *ApJS*, 199, 25
- Queyrel, J., Contini, T., Kissler-Patig, M., et al. 2012, *A&A*, 539, A93
- Refsdal, S. 1964, *MNRAS*, 128, 307
- Rhoads, J. E., Malhotra, S., Stern, D., et al. 2013, *ApJ*, 773, 32
- Ricotti, M., & Ostriker, J. P. 2004, *MNRAS*, 352, 547
- Robertson, B. E., Ellis, R. S., Furlanetto, S. R., & Dunlop, J. S. 2015, *ApJL*, 802, L19
- Rodney, S. A., Patel, B., Scolnic, D., et al. 2015, *ApJ*, 811, 70
- Rupke, D. S. N., Kewley, L. J., & Barnes, J. E. 2010, *ApJL*, 710, L156
- Schenker, M. A., Stark, D. P., Ellis, R. S., et al. 2012, *ApJ*, 744, 179
- Schmidt, K. B., Treu, T., Bradač, M., et al. 2015, *ApJ*, submitted
- Schmidt, K. B., Treu, T., Brammer, G. B., et al. 2014a, *ApJL*, 782, L36
- Schmidt, K. B., Treu, T., Trenti, M., et al. 2014b, arXiv:1402.4129
- Scoville, N., Aussel, H., Brusa, M., et al. 2007, *ApJS*, 172, 1
- Shapley, A. E. 2011, *ARA&A*, 49, 525
- Shapley, A. E., Reddy, N. A., Kriek, M., et al. 2014, arXiv:1409.7071
- Shapley, A. E., Reddy, N. A., Kriek, M., et al. 2015, *ApJ*, 801, 88
- Smith, G. P., Kneib, J.-P., Ebeling, H., Czoske, O., & Smail, I. 2001, *ApJ*, 552, 493
- Sobral, D., Smail, I., Best, P. N., et al. 2013, *MNRAS*, 428, 1128
- Stark, D. P., Ellis, R. S., & Ouchi, M. 2011, *ApJL*, 728, L2
- Steidel, C. C., Rudie, G. C., Strom, A. L., et al. 2014, *ApJ*, 795, 165
- Straughn, A. N., Kuntschner, H., Kümmel, M., et al. 2011, *AJ*, 141, 14
- Sullivan, M., Ellis, R., Nugent, P., Smail, I., & Madau, P. 2000, *MNRAS*, 319, 549
- Suyu, S. H., Treu, T., Hilbert, S., et al. 2014, *ApJL*, 788, L35
- Tacchella, S., Trenti, M., & Carollo, C. M. 2013, *ApJL*, 768, L37
- Tremonti, C. A., Heckman, T. M., Kauffmann, G., et al. 2004, *ApJ*, 613, 898
- Trenti, M., Bradley, L. D., Stiavelli, M., et al. 2011, *ApJL*, 727, L39
- Trenti, M., & Stiavelli, M. 2008, *ApJ*, 676, 767
- Trenti, M., Stiavelli, M., Bouwens, R. J., et al. 2010, *ApJL*, 714, L202
- Treu, T. 2010, *ARA&A*, 48, 87
- Treu, T., Ellis, R. S., Kneib, J., et al. 2003, *ApJ*, 591, 53
- Treu, T., & Koopmans, L. V. E. 2002, *MNRAS*, 337, L6
- Treu, T., Schmidt, K. B., Trenti, M., Bradley, L. D., & Stiavelli, M. 2013, *ApJL*, 775, L29

- Treu, T., Trenti, M., Stiavelli, M., Auger, M. W., & Bradley, L. D. 2012, *ApJ*, 747, 27
- Troncoso, P., Maiolino, R., Sommariva, V., et al. 2014, *A&A*, 563, A58
- Trump, J. R., Barro, G., Juneau, S., et al. 2014, *ApJ*, 793, 101
- Trump, J. R., Konidaris, N. P., Barro, G., et al. 2013, *ApJL*, 763, L6
- Trump, J. R., Weiner, B. J., Scarlata, C., et al. 2011, *ApJ*, 743, 144
- van Dokkum, P. G., Brammer, G., Fumagalli, M., et al. 2011, *ApJL*, 743, L15
- Vila-Costas, M. B., & Edmunds, M. G. 1992, *MNRAS*, 259, 121
- Vulcani, B., Poggianti, B. M., Finn, R. A., et al. 2010, *ApJL*, 710, L1
- Wang, X., Hoag, A., Huang, K., et al. 2015, *ApJ*, 811, 29
- Wright, S. A., Larkin, J. E., Graham, J. R., & Ma, C.-P. 2010, *ApJ*, 711, 1291
- Yagi, M., Gu, L., Koyama, Y., et al. 2015, *AJ*, 149, 36
- Yuan, T.-T., Kewley, L. J., & Rich, J. 2013, *ApJ*, 767, 106
- Zheng, Z., Cen, R., Weinberg, D., Trac, H., & Miralda-Escudé, J. 2011, *ApJ*, 739, 62
- Zitrin, A., Redlich, M., & Broadhurst, T. 2014, *ApJ*, 789, 51